Journal of
Materials Chemistry A

Multifunctional materials for photo-electrochemical water splitting

Journal:	*Journal of Materials Chemistry A*
Manuscript ID	TA-REV-03-2022-001869.R1
Article Type:	Review Article
Date Submitted by the Author:	14-Jun-2022
Complete List of Authors:	Rajaitha, Mary; DGIST, Robotics Hajra, Sugato; Daegu Gyeongbuk Institute of Science and Technology, Robotics Mistewicz, Krystian; Silesian University of Technology, Institute of Physics - Centre for Science and Education Panda, Swati; DGIST, Robotics and Mechatronics Sahu, Manisha; Daegu Gyeongbuk Institute of Science and Technology, Robotics Dubal, Deepak; Queensland University of Technology, Chemistry, Physics and Mechanical Engineering Yamauchi, Yusuke; University of Queensland, School of Chem Eng and AIBN Kim, Hoe Joon; Daegu Gyeongbuk Institute of Science and Technology, Robotics

Multifunctional materials for photo-electrochemical water splitting

[1]P Mary Rajaitha, [1]Sugato Hajra, [3]Krystian Mistewicz, [1]Swati Panda, [1]Manisha Sahu, [4]Deepak Dubal, #[5,6]Yusuke Yamauchi, #[1,2]Hoe Joon Kim

[1]Department of Robotics and Mechatronics Engineering, Daegu Gyeongbuk Institute of Science and Technology (DGIST), Daegu-42988, Republic of Korea

[2]Robotics and Mechatronics Research Center, Daegu Gyeongbuk Institute of Science and Technology (DGIST), Daegu-42988, South Korea

[3]Silesian University of Technology, Institute of Physics—Centre for Science and Education, Katowice 40-019, Poland

[4]Centre for Materials Science, School of Chemistry and Physics, Queensland University of Technology (QUT), 2 George Street, Brisbane, QLD 4001, Australia

[5]School of Chemical Engineering and Australian Institute for Bioengineering and Nanotechnology (AIBN), The University of Queensland, Brisbane, QLD 4072, Australia

[6]International Center for Materials Nanoarchitectonics (WPI-MANA), National Institute for Materials Science (NIMS), 1-1 Namiki, Tsukuba, Ibaraki 305-0044, Japan

 # Corresponding Authors Email:

Professor Hoe Joon Kim (joonkim@dgist.ac.kr)

Professor Yusuke Yamauchi (y.yamauchi@uq.edu.au)

Abstract

The energy crisis and depletion of non-renewable energy resources have been promoted due to the drastic rise in world pollution and the energy demand. Facile hydrogen production through water splitting has become a popular alternative source of energy owing to the numerous environmentally friendly and economic benefits it provides. Additionally, it is preferred due to the depletion of non-renewable energy resources, pollution caused by the burning of non-renewable energy resources, and climate change. Hydrogen fuel is generated from water by virtue and acts as clean energy without contributing to carbon emissions. Various water-splitting methods such as electrolytic, thermochemical, mechanocatalytic, plasmolytic, photocatalytic, and photoelectrocatalytic can be applied to obtain hydrogen and oxygen. This review highlights the multifunctional materials used in photo-electrochemical water splitting and their superior properties for producing carbon-free energy from water. The multifunctional materials help reduce aqueous protons to hydrogen and oxidize water to oxygen during the splitting of water. This paper discusses a wide class of materials such as carbon materials, metal-organic frameworks, perovskites, and semiconducting oxides for efficient hydrogen production. Different types of water-splitting methods and multifunctional materials with varying properties can lead to improved results. The review sheds light upon the hydrogen economy and future prospects, elucidating the selection of multifunctional materials for efficient hydrogen production.

Keywords: water splitting, metal-organic frameworks, perovskites, hydrogen economy.

1. Introduction

Energy has become an essential part of our daily lives, and some of its uses include consumer electronics and means of transportation. Fossil fuels such as coal, natural gas, and oil provide 81% of the primary energy supply and account for 61% of the electricity we use. The continuous rise in the human population and growth of various industry sectors around the globe keeps increasing the demand for energy [1,2]. The ever-increasing demand for more energy is directly related to the use of fossil fuels and the degradation of the environment. The continuous surge in the human population and the desire to improve living standards from 1950 onwards has resulted in increased energy demands. It is estimated that the current fossil fuel reserves can support the global economy for a limited time: petroleum for 40 years, natural gas for 60 years, and coal for 156 years [3–5]. The rapid depletion of these non-renewable energy resources poses a great danger to the economy worldwide. In addition, fossil fuel also poses a great threat to the environment, as they are not environmentally friendly due to the release of greenhouse gases and other pollutants. The release of these gases into the environment leads to several consequences, such as global warming and air pollution. The burning of fossil fuels increases the release of CO_2 into the environment, destroying the air we breathe. It is estimated that almost 100% of CO_2 released into the environment is due to burning fossil fuels or energy. The continuous release of these greenhouse gases into the environment leads to climate change and air pollution [6–8]. Therefore, it is necessary to find an alternative sustainable energy source. Thus, various studies have been conducted to find an alternative energy source due to economic and environmental concerns [9–11].

Hydrogen can be a promising alternative energy source but does not exist freely in nature. It is a secondary source of energy that can be generated from nature and bioresources. Hydrogen can play a great role in the future energy sector, thus fulfilling the global energy requirements and lowering CO_2 emissions. Hydrogen is a clean fuel and does not emit toxic by-products. It is considered the cleanest fuel and is eco-benign [12,13]. Among many technologies to generate hydrogen, photo-electrochemical (PEC) water splitting uses solar energy to split water into hydrogen and oxygen. Solar energy is a clean and inexhaustible source of energy. Figure 1 overviews different types of water splitting processes and multifunctional materials used in water splitting.

This review elucidates various water-splitting methods and, most importantly, focuses on multifunctional materials for PEC water splitting. Broadly, oxide semiconductors, perovskites, metal-organic framework, carbon materials, and 2-dimensional material for effectively harvesting sunlight and generating hydrogen with high efficiency by PEC water splitting.

2. Types of Water-Splitting Technologies

2.1. Electrolytic Water Splitting

Electrolytic water splitting is a process that uses two electrodes - a cathode for hydrogen evolution reaction (HER) and an anode for oxygen evolution reaction (OER), electrolyte, and a power supply to produce hydrogen and oxygen gases from water [14]. The electrodes and electrolytes used in the system are studied to increase the efficiency of electrolytic water splitting. Earth's abundant metals are studied as catalysts for electrolytic water splitting, IrO_2 and RuO_2 are used for the anode, and Pt is used for the cathode. These electrodes were studied at low pH of 1.6, and the voltage across the cell was 2 V; they showed a water-splitting activity for 24h. The catalysts were metastable and even acted as a short-time buffer by dissolving into an acidic medium without an applied bias to continue the gas evolution [15]. To increase the efficiency of the overall water splitting, the surface composite and morphology of a binary sulfide were studied. Here, binary Fe-

Ni sulfide was prepared on nickel foam by facile one-step electrodeposition, assisted by a liquid-crystal template (LCT). They were prepared in different morphologies and various composition ratios of Fe/Ni. The above study showed that binary sulfide had improved activity and conductivity compared to the single metal sulfide. The sample with a 3/1 ratio showed the best activity and excellent stability for overall water electrolysis [16], which is confirmed by the experimental data shown in Figure 2. The linear sweep voltammetry (LSV) curves (Fig. 2a), the overpotential (Fig. 2b), the Tafel plots (Fig. 2c), and electrochemical impedance spectroscopy (EIS) data (Fig. 2d) were registered for all materials electrodeposited in the water solution and LCT. A comparison of LSV curves for FeNi-S-3/NF deposited in water solution, and LCT is presented in Fig. 2e. During electrolytic water- splitting, hydrogen is produced along with oxygen gas and may suffer from gas mixing. To avoid the mixing of gases a low-cost conducting polymer material polyaniline (PANI) as a solid-state redox mediator for decoupling the OER and HER in acidic media was incorporated [17]. An electron-coupled proton buffer can also be used to separate the hydrogen and oxygen gas during electrolytic water splitting. Potassium hydroquinone sulfonate [18] and phosphomolybdic acid [19] were used as electron-coupled proton buffers to separate the gases during electrolytic water splitting. Different electrolyzers such as polymer electrolyte membrane (PEM) electrolyzer, alkaline electrolyzer, acid electrolyzer, and solid oxide electrolyzer are used in the electrolytic water splitting systems.

2.1.1. Polymer Electrolyte Membrane Electrolyzer

General Electric first developed the PEM electrolyzer in the 1960s to overcome the drawback of the alkaline electrolyzer. The main advantage of PEM electrolyzers is fast dynamic response time, reduced operational cost, large operational ranges, high efficiencies, and very high gas purities with greater safety and reliability [20,21]. The reactions, which take place at the PEM electrolyzer's cathode and anode, are described by the following equations.

$$\text{Cathode: } 2H^+ + 2e^- \rightarrow H_2$$

$$\text{Anode: } H_2O \rightarrow 2H^+ + 1/2O_2 + 2e^-$$

An anode and a cathode electrode are separated by solid plastic, which is responsible for the conduction of protons, the separation of gaseous products, and electrical insulation between the electrodes. Pt/Pd and IrO_2/RuO_2 metals are present at cathode and anode, respectively [22–25]. The water is pumped to the anode, where it is split into oxygen, electrons, and protons. The electron moves towards the external circuit, which is used as the driving force for the reaction. The protons move toward the cathode side through a proton-conducting membrane. At the cathode electrode, hydrogen is produced through the recombination of protons and electrons. This method is expensive, and the main challenge is to make it cost-efficient and maintain its efficiency [26,27].

2.1.2. Alkaline Electrolyzer

The alkaline electrolyzer is a well-established technology used in chemical industries for hydrogen production. Troostwijk and Diemann first introduced it in 1789. At the cathode, the two molecules, KOH and NaOH, are reduced to hydrogen and hydroxyl ions [20,28]. The reactions given below occur in the alkaline electrolyzer.

$$\text{Cathode: } 2H_2O + 2e^- \rightarrow 2OH^- + H_2$$

$$\text{Anode: } 2OH \rightarrow H_2O + 1/2O_2 + 2e^-$$

A difference in the operating principle of the alkaline and PEM water electrolysis cells is presented in Figure 3. In the case of an alkaline electrolyzer, hydrogen is eliminated from the cathode surface to a gaseous form, while hydroxyl ions are transferred to the anode through a porous diaphragm. In the anode, the 2-hydroxyl molecule is discharged to a half oxygen molecule and one water molecule. The oxygen escapes like hydrogen. The operating temperature of the alkaline electrolyzer is 30 - 80 °C, and the electrolyte used is an aqueous solution of KOH and NaOH with a concentration of ~20 - 30% [29,30]. The diaphragm in the middle of the cell separates the anode and cathode. It is also responsible for preventing the gases from mixing. The material used to construct the diaphragm, anode, and cathode are NiO, Ni/Co/Fe, and Ni/C-Pt, respectively. For the generation of one cubic hydrogen, the minimum energy required is 2.948 wK/h. A few disadvantages of this process are limited current density, low operating pressure, and low energy efficiency [31,32].

2.1.3. Acid Electrolyzer

The reverse reaction of the PEM electrolyzer is the acid electrolyzer, where the only difference is the catalytic material. An acid electrolyzer can be a potential corridor for hydrogen production. Citric, butyric, sulfuric, and phosphoric acids are used as electrolytes, and Pt wire is used as a cathode electrode [33]. The H^+ ions in the acid electrolyzer have formed the acids used as electrolytes.

$$\text{Cathode: } 2H^+ + 2e^- \rightarrow H_2$$

$$\text{Anode: } H_2O \rightarrow 1/2O_2 + 2e^- + 2H^+$$

Many studies have been conducted with various acid electrolyzers, and photocatalytic materials such as an anode and platinum, steel, or silver are used as a cathode for water splitting. First-row transition materials were also studied for an acid electrolyzer water-splitting system [15,34].

2.1.4. Solid Oxide Electrolyzer

Donitz and Erdle introduced a solid oxide electrolyzer in 1980 [35]. Solid ceramic material is used as an electrolyte to selectively conduct negatively charged oxygen ions at higher temperatures in a solid oxide electrolyzer. The electrolyzer should be sufficiently thick to prevent the exchange of steam and hydrogen gas which causes the recombination of H_2 and O^{2-}.

$$\text{Cathode: } 2H_2O + 4e^- \rightarrow 2O^{2-} + 2H_2$$

$$\text{Anode: } 2O^{2-} \rightarrow O_2 + 4e^-$$

Y_2O_3-doped ZrO_2 is an example of a solid oxide electrolyzer. ZrO_2 has unique properties such as high strength, high melting temperature, and excellent corrosion resistance. On fast cooling, Y_2O_3 minimizes the change in phase from tetragonal to monoclinic to prevent the formation of cracks, which can reduce the conductivity of the electrolyte. Scandia-stabilized and ceria-based electrolytes, lanthanum gallate materials, and scandium-doped chromate are other commonly used solid oxide electrolyzers [36]. A few interesting cathode materials that have been studied are Ni-doped Y_2O_3-doped ZrO_2, perovskite-type lanthanum strontium manganese, scandium-doped lanthanum strontium manganese, lanthanum strontium manganese chromate, and scandium-doped lanthanum strontium manganese chromate [37,38]. The main advantage of a solid oxide electrolyzer is that it can use the heat energy present at a higher temperature to produce hydrogen from water. Oxygen ions and hydrogen are produced at the cathode when water molecules react with the electron. These oxygen ions pass through the solid ceramic membrane, react with the anode from oxygen gas, and generate electrons for the external circuit [39]. The advantages of a solid oxide electrolyzer system are high storage capacity, minimal waste material disposal, high efficiency, long-term stability, fuel flexibility, low emission, and low operating costs. Despite this, a few disadvantages faced by this system are high operating temperature, leading to long start-up times, short lifetime and mechanical compatibility issues, and chemical instability caused by the diffusion between layers of the material [40].

2.2. Thermochemical Water Splitting

A thermochemical water splitting or thermochemical cycle is a process that involves the dissociation of the water molecule into hydrogen and oxygen through a repeated series of chemical reactions [41]. This process is not catalyst-dependent, and it only uses thermal energy. The thermochemical cycle driven only by thermal energy is called the pure thermochemical cycle. The thermochemical cycle uses other forms of energy sources, such as electrical, photonic, and solar, called hybrid thermochemical cycles [42]. In thermochemical water splitting, the water is decomposed into hydrogen and oxygen through repetitive reactions below 2,000 ℃ to avoid the very high temperature required for a single-step-thermochemical cycle [43]. In a two-step thermochemical cycle process, a metal oxide is reduced to release oxygen, which is an endothermic step. In the exothermic step, this oxygen reacts with water to produce hydrogen and pure oxygen, which is recycled in the first step [44]. The two-step thermochemical cycle requires a temperature of about 2,000 – 3,300 ℃ [45]. The main drawback of this process is that it shows a relatively low efficiency compared to electrolysis and requires a high temperature [46,47]. A three-step thermochemical cycle process can be established from a two-step process, in which the reaction with a higher temperature is replaced by a two-step process [48]. The most well-known cycle in the process is the Sulfur-iodine cycle. Its process consists of 1) a Bunsen reaction, an exothermic sulfuric acid production in the presence of water; 2) an endothermic decomposition of sulfuric acid; and 3) slightly endothermic decomposition of hydriodic acid [49]. The main drawback of this three-step thermochemical process is that it requires high temperature, and the reagents are harmful and corrosive [50]. The four-step thermochemical cycle consists of a hydrolysis reaction, a hydrogen-evolution reaction, an oxygen-evolution reaction, and a reagent-recycling reaction. The main advantage of this process is that it can work at a lower maximum operating temperature [51].

The hybrid thermochemical cycle is a process that uses both heat and other energy sources; the main advantage of this process is that the two-step process can work in lower temperatures [42]. The two-step hybrid sulfur (HyS) cycle is the most well-known hybrid process. It involves a two-step reaction, one step with thermal decomposition of sulfuric acid where heat is consumed and oxygen is produced and one electrochemical step for SO_2 electrolysis where electricity is consumed, and hydrogen is produced [52].

2.3. Mechanocatalytic Water Splitting

Mechanocatalytic water splitting is a process in which water is decomposed into hydrogen and oxygen using mechanical energy. The mechanical energy is converted to electrical energy and then to chemical energy. In the process, metal oxide powders such as NiO, Co_3O_4, Cu_2O, and Fe_3O_4. are dispersed in distilled water [53]. A Teflon-coated magnetic stirrer rod is used to agitate the dispersed powder. The dispersed powered rubbing between the stirring rod and bottom wall creates a frictional force along with the catalytic activity of the oxide material, which is responsible for water splitting. The rate of the evolution of gases is influenced by the stirring parameters, size, and material of the rod and the reaction vessel. The water splitting is due to the charge separation due to the friction generated between the catalytic particle and the bottom of the vessel, in which the catalytic powder and the reaction vessel get a negative and positive charge, respectively. This finding was challenged by much research, and an alternative explanation was provided [54]. There is no general agreement on the mechanism to date. A theory on the mechanism was proposed based on the experimental finding. The catalytic powder develops microcrevices because of the friction between the Teflon-coated rod and the surface of the glass vessel, leading to the development of a positive charge on the surface of the rod due to the loss of electrons and a negative charge on the glass vessel. The oxide particles in microcrevices are subjected to a high electric field. Negatively charged oxygen atoms are formed by the oxygen trapped in the interstitials of the oxide particles, which are negatively charged due to obtaining electrons and leaving the neighboring metal ions with positive holes. These electron and holes are responsible for water splitting. The electron is transferred to the rod and then to the glass surface. The protons combine with these electrons to form hydrogen at the bottom of the glass vessel. These holes oxidize water and generate oxygen and protons at the rod. The rod and the glass vessel act as anode and cathode, respectively [55].

2.4. Plasmolytic Water Splitting

Plasmolytic water splitting is a process that uses the electric discharge of plasma without acquiring high temperatures. In this process, the electric energy is converted into kinetic energy of the electron and then to the kinetic energy of the heavy particles. Hot and cold discharge are two types of plasma discharge [56]. Water splitting through water plasmolysis and CO_2 plasma/CO +H_2O are the two mechanisms used for water splitting. In water-splitting through water plasmolysis, water is decomposed through a vibrationally excited state and dissociative attachment route [57]. The main disadvantage of this method is that it requires a high ionization degree, which is hard to attain. In the CO_2 plasma/CO +H_2O method for hydrogen production from water, CO_2 acts as a cocatalyst because it reduces the need for high degrees of ionization and decreases the concentration of OH free radicals. Without the CO_2 catalyst, the efficiency was only 50%, but with the CO_2 catalyst, the efficiency increased to 80%, and it also needs a lower degree of ionization. This process has an additional advantage after separation as it produces hydrogen and can form methanol and many other substances depending on the conditions. A few limitations of this process are low hydrogen production rate, costly large-scale hydrogen production, and utilization of electric power [57].

2.5. Photocatalytic Water Splitting

Photocatalytic water splitting has been widely studied to produce hydrogen and oxygen cost-effectively [58–61]. It can produce renewable energy and has no CO_2 emissions. An oxidation-reduction reaction takes place at the interface when a photocatalytic material is introduced into the water without any electrical work. To split the water, the valance and conduction band of the material should match with the oxygen and hydrogen evolution potential [62–65]. There are two primary approaches to splitting water in a photocatalytic system. In one approach, a single material is used to split water into hydrogen and oxygen. The material used should have a sufficiently narrow bandgap, a suitable thermodynamic potential, and stability against corrosion [66]. Another approach is to use two different photocatalytic materials with a two-step excitation mechanism. The main advantages of this process are that it has a low process cost and the ability to separate hydrogen and oxygen during the reaction. In addition, it requires a small reactor system and a reasonable solar-to-hydrogen efficiency [67,68].

2.6. Photo-electrochemical (PEC) Water Splitting

Solar energy is the most abundant, clean, and renewable energy source. A promising technology to utilize this solar energy is hydrogen fuel production through PEC water splitting [69–71]. Henri Becquerel first observed this phenomenon; he reported that sunlight acted on sliver chloride coated platinum electrode produced photocurrent and photovoltage in different electrolytes. The photochemical reaction cannot be stimulated in pure water as it only absorbs the infrared region, and the photon energy is low to stimulate a photochemical reaction. Therefore, to decompose water, a semiconductor with a small bandgap or a wide bandgap semiconductor with a sensitizer or cocatalysts in the presence of sunlight and electric energy is used. In this process, hydrogen and oxygen are generated through the decomposition of water because of the photochemical reaction started by the semiconductor after the adsorption of sunlight [72–77]. The PEC water splitting process is one of the most promising methods to convert light energy into chemical energy. The main challenge in the PEC system is to find a suitable material with absorption on a broad range of the solar spectrum, high stability in photochemical, suitable band edge position, low overpotential, efficient use in photogenerated electron-hole pair, and low cost. It is difficult to achieve everything in a single semiconductor. Therefore, extensive research is going on to combine different semiconductors to achieve a suitable material with high efficiency [78–80]. Various materials such as semiconductors, perovskites, metal-organic framework, and 2-dimensional materials have been studied.

3. Fundamental Understanding of the PEC Mechanisms

PEC water splitting is a process in which the water is split into hydrogen and oxygen in the presence of sunlight and bias, as depicted in Figure 4a. In this process, the hydrogen is produced by exploiting the solar irradiation that hits the Earth's surface [81]. The light energy is converted into chemical energy, and water undergoes a reduction and oxidation reaction when hydrogen and oxygen are split. A photocatalytic material consists of a conduction band and a valance band separated by a bandgap [13,82]. When the material absorbs light energy greater than its bandgap energy, the electron from the valance bands gets excited in the conduction band, creating a hole in the valance band, as depicted in Figure 4b. These photogenerated electron and hole pairs take part in an oxidation-reduction reaction that splits water into hydrogen and oxygen. In the oxidation reaction, water is split to form H^+ ions, and in the reduction reaction, these H^+ ions gain an electron and become H_2. For the redox reaction to occur, the reduction and oxidation potential should be above and below the conduction band and valance band [83,84]. There are two types of water splitting systems: a single-component system and a multi-components system. In a single-component system, the oxidation and reduction reaction occurs in the same semiconductor particle, and the conduction and valance band of this semiconductor must have the thermodynamical potential for the oxidation and reduction reaction to occur. In the multi-components system, the two semiconductors form a heterojunction. When the semiconductor absorbs enough photon energy, the electron from the valence band gets excited to the conduction band to the reduction cocatalyst, where the reduction reaction occurs. The excited electron leaves behind a hole that diffuses in the valance band to the oxidation cocatalyst, where the oxidation reaction occurs. The redox-mediated in the dual particle system relaxes the constraints, as the voltages of both particles sum up to provide the driving force for overall water splitting [10, 72].

3.1. Factor Affecting Efficiency of the PEC

3.1.1. Photocurrent

The bandgap energy of the semiconductor is used to determine the photocurrent density of the photoelectrode. A low photocurrent is due to the electrical losses, because of which the photogenerated charges are unable to contribute to the electrochemical reaction. Few methods to enhance the photocurrent of the material are heteroatom doping, adjusting morphologies and orientations, thickness control, and one-dimensional nanostructuring, reducing reflection, and reducing resistance. The doping method can enhance the optical and electrical properties of various materials. Mo and W doped $BiVO_4$ showed that as the donor concentration increases, there was an increase in the conductivity of the material [86]. Hydrogen and nitrogen doping in $BiVO_4$ increased the photocurrent of the material, and Mo and nitrogen doping in $BiVO_4$ increased the photocurrent density [87,88]. These are confirmed by the experimental data shown in Figure 5. An increase in photocurrent density for water oxidation at 0.6 V versus reversible hydrogen electrode (RHE) was observed due to the nitrogen treatment of $BiVO_4$ (Fig. 5a). The J–V curve was registered for N_2-treated $BiVO_4$/FeOOH/NiOOH (Fig. 5b) using a two-electrode cell to determine the applied bias photon-to-current efficiency (ABPE), which attained a high value of 2.2% at 0.58 V (Fig. 5c). The ratio of hydrogen to oxygen generation was 1.81:1 (Fig. 5d), which was attributed to the leak of H_2 during its manual sampling for gas chromatography analysis [88]. The time dependence of photocurrent density was registered at 0.6 V versus RHE to compare the long-term stability of N_2-treated $BiVO_4$/FeOOH/NiOOH for water and sulfite oxidation (Fig. 5e). Similarly, Co and Sn co-doped Fe_2O_3 showed an enhanced photocurrent density compared with pure Fe_2O_3 [89]. WO_3 doped with Bi also showed an increase in the photocurrent [90]. The morphology and the crystalline orientation can affect the photocurrent density when the semiconductor mater a strong electrical property depending on crystalline orientation. The photocurrent density of $BiVO_{4,}$ which has an orientation [010], was found to be higher than the [001] orientation due to the significant increase in the charge transport [91]. Sb_2Se_3 prepared in three different mixing ratios of thioglycolic acid to ethanolamine by solution processing showed a different photocurrent density. The high photocurrent density was seen in well-aligned short Sb_2Se_3 nanorods along the vertical [001] direction [92]. The thickness of the material determines the number of photons absorbed. To fully absorb the solar spectrum, the thickness should be large than the penetration of depth of the incident light. If the diffusion length of the minority carrier is shorter than the thickness of the semiconductor, the photo-excited charge carriers recombine. The vertically aligned Ta_3N_5 nanorods showed a photocurrent density 3.2 times higher than the planar Ta_3N_5 because of the short charge carrier diffusion length [93]. Reducing surface reflection by multiple scattering enhances light absorption. A nanoporous black Si prepared by metal-assisted etching showed a high photocurrent density of 1.2 times higher than polished Si as it reduces the reflectivity [94].

The undesirable resistance in the PEC system can reduce the photocurrent density. In a CdS/CIGS photoelectrode and Pt catalyst system, a thin Mo/Ti metallic layer between the CdS/CIGS photoelectrode and Pt catalyst increased the photocurrent by approximately 20%. The Ti layer made intimate contact with CdS/CIGS photoelectrode, and Mo assisted in the uniform deposition of Pt catalyst [95].

3.1.2. Photovoltage

The difference in the Fermi level between the two solid-state materials gives rise to photovoltage. In the case of photoanode improving onset, potential means to shift the onset potential towards the negative voltage, and in the case of photocathode, it means shifting towards the positive voltage. Passivation of surface state, improving band alignment, and depositing catalytic overlayers are a few methods to improve the photovoltage of the PEC materials. An example of surface-state-induced photovoltage loss is Fe_2O_3. The onset was decreased as much as 100 mV upon the deposition of the ultrathin ALD layer, while the deposition of TiO_2 with the same thickness showed no improvement. The deposition of Co^{2+} ions decreases the onset potential even more [96]. Further studies stated that the deposition of the passive layer was responsible for the decrease in the onset potential. To achieve high photovoltage, it is important to choose an appropriate heterojunction layer. One of the well-studied photocatalytic materials is Cu_2O, which showed an enhancement in photovoltage when it formed a composite with Ga_2O_3 compared to the composite formed with AZO. The increase in the photovoltage is 5 times higher than AZO/Cu_2O-based photocathode [97]. Another way to increase the photovoltage is by depositing catalytic overlayers.

3.1.3. Material Stability

One of the main challenges of the PEC system is the stability of the material. The cause of instability is due to the photo corrosion of the semiconductor material, which occurs when the photogenerated charge carrier drives self-oxidation rather than water splitting. The use of materials that are stable against corrosion can achieve stability. Another cause of instability is the poor interfaces of the semiconductor, catalysts, and electrolytes. To increase the stability, a protective layer that can separate the semiconductor from the electrolyte is used. ALD-TiO_2 layers were studied by the various groups, which showed that the ALD-TiO_2 used in Cu(In, Ga)(S, Se)$_2$ (CIGS) photocathodes (NiMo/TiO_2/CdS/CIGS) was stable in various pH conditions [98]. TiO_2 on top of a p-type semiconductor increases the photocurrent and onset potential, as it acts as a protective layer and n-type overlayer. Many materials other than TiO_2 have been studied to be used as a protective layer. An Al_2O_3 layer was used as a protective layer for GaN photoelectrode and showed a slight decrease in the photocurrent due to high resistance after the deposition of Al_2O_3. However, the photocurrent density of the Al_2O_3 coated sample maintained a constant value while the bare GaN showed a rapid decrease in the photocurrent density [99]. Electrolytes can also affect the stability of the material. It can be reduced by tuning the composition of the electrolyte and controlling the dissolution reaction. In the $BiVO_4$ photoanode system, V^{5+} was added to the electrolyte in the form of V_2O_5 for long-term stability. It was noted that after the addition of V_2O_5, it showed a stable photocurrent density without a noticeable decrease for 60 h. The X-ray diffraction (XRD) showed no change after the stability test. Without the addition of V_2O_5, there was a decrease in the XRD peak after the stability test [100].

4. Oxide Semiconductor For PEC Water Splitting

Titanium dioxide (TiO_2) has been widely studied for its application in PEC water splitting due to its stability against photo corrosion and chemical corrosion; additionally, it incurs low cost and is photoactive [101–103]. The bandgap of TiO_2 is 3.2 eV limiting its photoactivity to ultraviolet (UV) energy, and it has a high recombination rate of photogenerated current carriers, reducing its efficiency. Various methods such as doping and semiconductor coupling have been employed to improve the bandgap and efficiency of TiO_2 [104,105]. A Ni-doped TiO_2 nanotube was prepared by anodizing different Ti-Ni alloys and further annealing them at a high temperature. The prepared Ni-doped TiO_2 showed a photoconversion efficiency of 0.67%, which was 3.35 times higher than the photoconversion efficiency of pure TiO_2. The 3d state of Ni was introduced into the forbidden band and acted as a trapping site preventing the recombination of photogenerated charge carriers; as a result, it increased the photoconversion activity of TiO_2. The UV spectra of the prepared sample showed that the optical absorption of the TiO_2 increased upon the doping of Ni, and a redshift was absorbed with the increase of Ni doping. From the PL spectra, it was observed that the PL intensity of the Ni-doped samples showed less intensity compared to undoped TiO_2; this is due to the longer electron lifetime induced by Ni doping [106]. TiO_2 nanocavity arrays [107] were prepared by anodization, and the Al film was deposited in the nanocavity array, followed by thermal dewetting, as shown in Figure 6. The generated electron-hole pair separates at Al/TiO_2 interface, then the electron injects into the conduction band, and the holes are utilized in the oxidation of water. The Al/TiO_2 showed an enhanced photocatalytic water splitting activity compared to pure TiO_2. The high-resolution transmission electron microscopy (HR-TEM) and scanning electron microscopy (SEM) images showed the formation of heterostructured Al@TiO_2. The UV spectra of the prepared sample showed a plasmonic absorption peak which attributes to the localized surface plasmon resonance (LSPR) effect and electromagnetic field polarization [107].

Tungsten trioxide (WO_3) is an n-type semiconductor with a bandgap of about 2.5 ~ 2.8 eV, which is approximately 2% of the solar spectrum. They are Earth-abundant, highly tunable and chemically stable, and have excellent electrical conductivity [108,109]. Bi-doped WO_3, prepared using a hydrothermal method, was studied for its PEC water splitting capabilities. Bi-doped WO_3 showed four times enhanced performance when compared to undoped WO_3. The doping of Bi showed a downward shift in the Fermi level and increased the bandgap. The downward shift observed in the valance band is expected to increase the PEC efficiency, which was observed in UV spectra. The TEM study observed that the Bi doping did not induce any structural change and showed a homogeneous embedding of Bi [90]. The hydrothermal method was used to prepare Sn-doped WO_3 for PEC water splitting [110]. The Sn-doped material showed enhanced photocatalytic activity (Figure 7) due to the increase in oxygen vacancies and reduction in the bandgap. The increase in the oxygen vacancies increased the donor density levels in WO_3, which increased the PEC performance. The TEM results showed the evenly distributed Sn ions in WO_3 lattices. A redshift was absorbed in the UV spectra, and the doping of Sn caused a tailing of absorbance onset into the visible region, indicating the increase in oxygen vacancies [110]. The hydrothermal method was used to grow Mo-doped WO_3 on a fluoride-doped tin oxide glass substrate. The prepared material showed an enhanced PEC activity compared to pure WO3, which can be attributed to the reduction in bandgap upon introducing Mo and the increase in charge carrier density. The UV spectra showed a decrease in the bandgap position upon the addition of M_O [111].

Cuprous oxide (Cu_2O) has been extensively studied for its application in PEC water splitting due to its conductivity which is dominated by copper vacancies. It has a bandgap of about 2.0 eV, and it is nontoxic. However, the poor stability and low migration rate of Cu_2O affect their PEC efficiency [112–114]. The electrochemical deposition method was used to grow Cu_2O films on the fluorine tin oxide substrate, and g-C_3N_4 was deposited on the Cu_2O film by an electrophoretic deposition process. The PEC water-splitting study shows that the PEC performance of the Cu_2O/g-C_3N_4 heterojunction was better than pure Cu_2O and g-C_3N_4. They showed a photocurrent density and PEC hydrogen evolution efficiency of -1.38 mA/cm^2 and 0.48 mLh^{-1}cm$^{-2,}$ respectively. The XRD results showed the formation of the heterojunction between g-C_3N_4 and Cu_2O, which is ideal for the charge transfer, and it reduces the recombination of photogenerated electron-hole pairs; and enhances the PEC efficiency [115]. Electrodeposition was used to grow Cu_2O film in an aqueous solution of varying pH and studied for its PEC water splitting ability (Figure 8). The film grown in pH 12 showed the highest PEC efficiency [116]. Cu_2O micro/nanostructure film was synthesized on copper foil by a facile and cost-effective template route through the transformation of a lotus-like CuO/Cu(OH)$_2$ nanosheet/nanowire structure. The prepared material showed a photocurrent of -1.6 mAcm^{-2} at a potential of -0.6 V, and a solar conversion efficiency of 1.97% [117].

Zinc oxide (ZnO) is a direct wide bandgap semiconductor with a bandgap of about 3.37 eV. ZnO materials have been studied for their PEC water splitting ability owing to their excellent electron mobility and transfer efficiency, intrinsic stability, and favorable environmental compatibility [118,119]. The chemical route was used to grow ZnO nanoparticles on a multi-walled carbon nanotube (MWCNT) surface. ZnO/MWCNT showed 5 times more photocurrent density when compared to pure ZnO (Figure 9a), this increase in photocurrent is attributed to the decrease in band-bending and effective interfacial electron transfer. Moreover, a smaller arc radius of ZnO/MWCNT was observed in the EIS Nyquist plot as compared to that of pristine ZnO (Figure

9b). It proved that MWCNT is beneficial for the separation of photogenerated charge carriers. It was confirmed from the TEM and SEM images that ZnO nanoparticles were uniformly dispersed on the surface of MWCNT without any aggregation of ZnO [120]. ZnO/Au heterostructure was prepared through the heterostructure and photoreduction combined method. The prepared heterostructure showed a photocurrent density of about 9.11 mA/cm^2 and hydrogen conversion efficiency of the heterostructure of 0.48%, which are much higher than pure ZnO. The enhanced performance is due to a defined interface between ZnO and Au. It was observed from SEM and TEM images that the tip of the ZnO nanorods was covered with Au nanoparticles. The UV spectra of the heterostructure showed that the bandgap of the ZnO extended to visible light after the deposition of Au. The bandgap transition of ZnO strengthened the absorption intensity. A great decrease in the PL intensity was observed after the deposition of Au due to the electron trapping effect [121]. ZnO/CdS/Au nanotubes arrays were prepared through the chemical bath deposition method followed by sulfuric acid corrosion. The prepared nanotube arrays showed a photocurrent density of 21.53 mA/cm^2 at 1.2 V and photoconversion efficiency of about 3.45% under visible light irradiation. The type II bandgap structure between ZnO and CdS increases the photocatalytic activity by decreasing the recombination of the rate of photoinduced electron-hole pair. The formation of a hexagonal nanotube hollow structure was observed from SEM and TEM imagining [122].

Ferric oxide (Fe_2O_3) is an n-type semiconductor with a bandgap of about 2 to 2.2 eV. It depicts high stability in an aqueous solution. It is non-toxic, environmentally friendly, and present in abundance [123,124]. Its photocatalytic efficiency has been limited due to low electron mobility, short hole diffusion length, and short lifetime of charge carriers [125,126]. Ultrathin NiMn-layered double hydroxide nanosheets coupled with α-Fe_2O_3 nanorod arrays were prepared through a hydrothermal method. The prepared photocatalytic material showed a photocurrent density of 1.98 mA cm^2, which is 11 times higher than pure Fe_2O_3. The enhanced PEC efficiency is due to the improved interfacial charge separation and electron transportation observed in PL and electrochemical impedance studies. It was seen in the TEM image that the α-Fe_2O_3 nanorod was fully covered by a thin layer of NiMn [127]. α-Fe_2O_3 nanoflowers were prepared by an aerosol-assisted chemical vapor deposition method. The prepared nanostructure showed a photocurrent density of up to 585 μA/cm^2. The nanoflower showed an efficient charge carrier separation and lower charge transfer resistance at the photoanode/electrolyte interface. The SEM and TEM studies revealed that the nanoflower structure was formed by the stacking of nanoflakes [128]. The electrodeposition method was used to deposit nanostructured α-Fe_2O_3 thin film. The thin film showed a photocurrent density of 0.67 mA/cm^2 at 1.23 V versus reversible hydrogen electrode (RHE) under standard illumination conditions [129].

5. Perovskites Material For PEC Water Splitting

Lanthanum iron oxide ($LaFeO_3$) has a bandgap of 2.1-2.6 eV and is a visible light response material [130,131]. It has been studied for its application in water splitting, dye decomposition, and CO_2 reduction due to its photocatalytic capability, optical characteristics, and good stability in water [132–134]. Magnetron sputtering method was used to prepare $LaFeO_3$ on the surface of g-C_3N_4. The hydrogen production of prepared material was found to be 10.8 μmol h^{-1} cm^{-2} under visible light irradiation, which was 70% higher than pure $LaFeO_3$ and g-C_3N_4. The enhanced PEC performance resulted from efficient charge separation due to the formation of the heterostructure. The XRD study confirmed the formation of the heterostructure; it showed both the peaks corresponding to $LaFeO_3$ and g-C_3N_4 [135]. $BiVO_4$/Co-$LaFeO_3$ composite was electrodeposited on the FTO glass by electrodeposition method and studied for its PEC performance. The prepared composite showed a photocurrent of about 3.4 mA/cm^2. The enhanced PEC performance of the prepared composite was due to the reduced recombination rate of the prepared material and the surface passivation effect of Co-substituted $LaFeO_3$. The deposition of Co-$LaFeO_3$ clusters on the surface of $BiVO_4$ was observed from the SEM image. The HR-TEM image also confirmed that the surface of $BiVO_4$ is packed with Co-$LaFeO_3$ clusters [136].

Calcium titanate ($CaTiO_3$) is an orthorhombic structure perovskite with a wide bandgap range of 3.6 eV. The one-pot hydrothermal method was used to prepare a hierarchical architecture of $CoTiO_3$ constructed from a single crystal nanowire [137]. The hydrogen generation rate of the prepared material was 14.19 μmol h^{-1} g^{-1} (Figure 10). The enhanced PEC performance of the prepared material is due to the formation of oxygen vacancies that acted as electron donors and increased the separation of photogenerated charge carriers. The SEM image showed that the prepared material had a higher specific surface area with more active sites, thus increasing the PEC performance [137]. g-C_3N_4/$CaTiO_3$ heterojunction was prepared through the hydrothermal co-deposition method. The prepared material showed an enhanced PEC performance that was 18 times higher compared to unmodified materials. The increase in the PEC performance is due to the formation of nano-heterojunction between g-C_3N_4 and $CaTiO_3$, which is responsible for promoting the transfer of photoinduced electrons and holes, providing efficient charge separation, and increasing the lifetime of charge carriers. An increase in the visible light absorption after the formation of the heterojunction was observed from the UV spectra. The deposition of g-C_3N_4 on the surface of $CaTiO_3$ was seen in the SEM image, indicating the heterojunction formation [138].

Tin zinc oxide ($ZnSnO_3$) has a wide bandgap of 3.25 eV with high visible transmittance and electron mobility [139,140]. The electrophoretic deposition method was used to prepare the

$ZnSnO_3/MoS_2$ heterostructure. The photocurrent density of this electrode is 2.3 times and 27.3 times higher than the pure $ZnSnO_3$ and pure MoS_2, respectively. The enhancement in the PEC performance is due to the formation of type II heterostructure, which improved the separation of photogenerated charge carriers and reduced the recombination rate. The SEM image showed that the MoS_2 nanosheet was randomly dispersed on the surface of the $ZnSnO_3$ layer. The formation of the heterostructure was confirmed for the XRD spectra [141]. $Cu(In, Ga)S_2/In_2S_3$ on $ZnO/ZnSnO_3$ was prepared using spray pyrolysis. The prepared heterojunction showed a photocurrent density of about 6.4 mA cm^{-2}, which was 3 times higher than the $ZnO/Cu(In, Ga)S_2/In_2S_3$ electrode. The formation of heterostructure reduced the recombination of photogenerated electrons and holes, increasing the PEC performance. The SEM image showed nanosheet structure formation [142].

Sodium tantalate ($NaTaO_3$) has proved to be an excellent candidate for PEC water splitting under UV light irradiation with a bandgap of about 4 eV [143,144]. The chronopotentiometry method was used to incorporate RuO_2 on $NaTaO_3$ film. The prepared sample showed an enhanced PEC performance. Under visible light irradiation, it achieves a maximum hydrogen production of 15.7 mmol h^{-1} g^{-1} and solar-to-hydrogen conversion efficiency of 4.29%. The enhanced performance is due to the efficient charge separation of photogenerated electrons and holes and the low recombination rate of charge carriers. Two different morphologies were observed for the RuO_2-$NaTaO_3$ electrode in SEM imaging. It was observed from the UV spectra that the visible light absorption increased with an increase in RuO_2 content [145]. The solid-state method was used to create $NaTaO_3$ and $BaBiO_3$, and the $NaTaO_3/BaBiO_3$ heterojunction was formed through the wet impregnation method. The prepared heterojunction showed the highest hydrogen production of 54 μmol g^{-1}, which was 1.4 times higher than pure $NaTaO_3$. The increase in the PEC performance was due to the formation of heterojunction, which enhanced the transfer of photoinduced charge carriers and reduced the recombination of charge carriers. The SEM image showed the formation of heterostructure between $NaTaO_3$ and $BaBiO_3$. It clearly depicted the presence of two different particles in the composite. A redshift was observed in the UV spectra, which showed the enhancement in visible light harvesting [146].

Silver vanadium oxide ($AgVO_3$) has a narrow bandgap of 2.3 eV, and it has been studied for various applications like photocatalysis, lithium batteries, and photoluminescence materials [147,148]. The co-precipitation method was used to prepare the MoS_2/Ag-$AgVO_3$ heterostructure. The prepared heterostructure showed a hydrogen generation of 38.6 mmol g^{-1}, which was 4 times higher than Ag-$AgVO_3$ and 20 times higher than MoS_2. The enhanced PEC performance was due to the increased separation and transfer of photoinduced charge carriers. An interconnected architecture was observed for the heterostructure under the TEM image. It showed that the Ag-$AgVO_3$ nanorods were dispersed on the surface of the MoS_2 nanosheet. The UV spectra showed that the absorption edge of the heterostructure shifted to the IR region after the formation of the heterostructure [149]. It was found in [149] that the type-II heterojunction charge-transfer mechanism may not be possible for MoS_2/Ag–$AgVO_3$ heterostructures (Figure 11a). The band structures, calculated from the Mott-Schottky study, demonstrated a Z-scheme interfacial charge-transfer mechanism (Figure 11b). The $AgVO_3$/Mo-$BiVO_4$ heterostructure was prepared through a simple successive ionic layer adsorption and reaction method. The prepared heterostructure showed a photocurrent density 7 times higher than pure $BiVO_4$. The charge injection efficiency was increased to 49%, which was 5 times higher than pure $BiVO_4$. The increase in the performance is due to the formation of heterostructure, which increased the charge separation and increased the oxygen vacancy on the surface. The TEM and HRTEM image of the heterostructure showed that

$AgVO_3$ was loaded on Mo-$BiVO_4$ successfully and presented as overlapped small nanoparticles. The UV spectra showed that the formation of heterostructure improved the absorption edge [150].

6. Metal-Organic Framework for PEC Water Splitting

ZnO@ZIF-8/67 was prepared by ZIF-8 bridging ZnO and ZIF-67 through the hydrothermal method. The prepared material showed a photocurrent density of 0.11 mA cm^{-2}, which was 9.2 times higher than pure ZnO. The enhanced performance exhibited by the material is due to the fast one-dimensional electron transfer on the ZnO nanorods and the high visible light absorption of ZIF-67. The SEM image of ZnO@ZIF-8/67 was shorter than the pristine ZnO, which indicates an etching effect to form ZIF-8/67 as a linker between ZnO and ZIF-64. A core-shell structure of ZnO@ZIF-8/67 was seen in the TEM image. A short absorption peak was observed in UV spectra [151]. The solvothermal method was used to prepare a ZnO nanotube with nitrogen-doped carbon dots embedded in ZIF-8. The prepared material showed enhanced photocurrent density compared to pure material due to the increase in several photogenerated electrons and holes from the enhanced visible light absorption of nitrogen-doped carbon dots. The formation of the ZnO nanotube with nitrogen-doped carbon dots embedded ZIF-8 was confirmed through TEM and SEM images. The UV spectra showed that the prepared material had a redshift towards the visible light region [152].

MIL-53(Fe) catalyst-modified Mo:$BiVO_4$ film was prepared through the spin coating. The prepared material showed a photocurrent density of 2.2 mA cm^{-2}, which was 4 times higher than the pure material. The enhanced PEC performance is due to the formation of heterojunction between Mo:$BiVO_4$ and MIL-53, which prevented the recombination of photogenerated electrons and holes. The photoconversion efficiency increases with a reduced recombination rate. The SEM and TEM images showed the formation of MIL-53 on the surface of Mo: $BiVO_4$. The UV spectra showed that the absorption edge of the prepared material was higher than pure MIL-53 [153]. Fe-doped $BiVO_4$ modified with MIL-53(Fe) was prepared by spin coating. The prepared material showed a photocurrent of 1.15 mA/cm^2, which was much higher than the pure material. The enhanced PEC performance is due to the MIL-53, which facilitates the charge separation efficiency and enhances performance. The SEM study revealed the formation of MIL-53 on Mo:$BiVO_4$. A redshift was observed for the prepared material in UV spectra [154].

The chemical vapor deposition (CVD) method was used to decorate Fe_2O_3 nanorod arrays with MIL-101. The prepared material showed a photocurrent density of 1 mA cm^{-2}, which was 2.5 times higher than pure Fe_2O_3. The exciton lifetime and the electrochemically active surface area were also 14 and 1.3 times higher than the pure material. The increase in the PEC performance is due to the reduced recombination of charge carriers in the MIL-101 layer. The SEM and TEM images showed the formation of MIL-101 on top of Fe_2O_3 [155]. The Fe_2O_3/MIL-101 heterostructure film (Figure 12) was prepared through a one-drop method under hydrothermal conditions [156]. The photocurrent density exhibited by the prepared material was 20 $\mu A \cdot cm^{-2}$, which was 2 times higher than pure Fe_2O_3. The enhanced PEC performance is due to the formation of type II heterostructure, which reduced the recombination rate of the photogenerated charge carriers. The heterostructure formation was confirmed by the SEM image and energy dispersive X-ray (EDX) elemental mapping. The UV spectra showed that the absorption edge of the heterostructure moved towards about 490 nm [156]. The EIS studies of Fe_2O_3 (Figure 13a) indicated that the mass transfer process determined the surface reaction kinetics. Therefore, PEC water oxidation efficiency was limited. In the case of the Fe_2O_3/MIL-101 film, the increased slope of the straight line was observed in the EIS Nyquist plot (Figure 13a). It suggested the enhanced reactant diffusion rate and water oxidation kinetics. Transient photocurrent responses of Fe_2O_3 and Fe_2O_3/MIL-101 at 0.6 V under continuous illumination were measured to examine the stability of the samples (Figure 13b). It was noted that the photocurrent density of Fe_2O_3/MIL-101 decreased gradually after 500 s. It was attributed to the insufficient quality of the connection between the Fe_2O_3 film and the layer of the metal-organic framework. The Fe_2O_3/MIL-101 was further investigated using XRD (Figure 13c), Raman spectroscopy (Figure 13d), SEM, and EDX (Figure 13e) to characterize the structural modification after completion of all PEC experiments. No significant changes in the crystal structure and composition of the Fe_2O_3/MIL-101 were observed when the PEC studies were completed.

The hydrothermal method was used to prepare NH_2-MIL-125(Ti) incorporated TiO_2. The photocurrent density of the prepared material is 3.04 mA cm^{-2}, which is higher than pure materials. The prepared material showed the highest hydrogen production rate of 132.86 μmol h^{-1} cm^{-2}. The enhanced PEC performance was due to the excellent light utilization, and it promoted charge separation and long-term photostability because of the heterostructure formation. The formation of the heterostructure was seen in the TEM image [157]. NH_2-MIL-125(Ti)/TiO_2 was prepared by the hydrothermal method and showed a high photocurrent density of 1.63 mA/cm^{-2}, which was 2.7 times higher than pure TiO_2. The photon-electron conversion efficiency was about 84.4%. The enhanced PEC performance was due to the formation of type II heterostructure, which promotes efficient light absorption and charge separation. Perpendicular growth of the sample was observed in the SEM image [158].

UiO-66/Pd/S, N graphene quantum dots were prepared for the PEC water-splitting study. The prepared material showed a photocurrent density of about 297 μA cm^{-2}, a photon-to-current efficiency of 0.66%, and the absorbed photon-to-electron conversion efficiency of 19.7%. The enhanced PEC performance is due to the higher separation and low recombination rates of electrons and holes. It was observed from the SEM image that the surface of UiO-66 was covered with quantum dots indicating the formation of the composite. The TEM and HRTEM images showed that Pd nanoparticles were grown on the UiO-66 surface, and S, N graphene quantum dots covered both surface deposit Pd nanoparticles and UiO-66 [159]. The UiO-66@$ZnIn_2S_4$ nanocomposites with UiO-66 nanoparticles being encapsulated by $ZnIn_2S_4$ nanosheets were fabricated. The prepared hybrid material generated hydrogen at the rate of 3061.61 μmol h^{-1} g^{-1} and had a quantum efficiency of 9.84%. It was observed from the FESEM image that the nanosheet was uniformly dispersed on UiO-66 nanoparticles. The TEM image also showed that the UiO-66 nanoparticle was encapsulated by the nanosheet [160].

ZnO@ZIF-8/67 encapsulated ZnO nanorod array was synthesized on the FTO glass substrate and was investigated for its PEC water splitting. The prepared material showed a photocurrent density of 0.11 $mAcm^{-2}$. The photocurrent density exhibited by ZnO@ZIF-8/67 was 9.2 times higher than the pristine ZnO nanoarrays. The enhanced PEC activity is due to the fast electron transportation in one dimension and the intense visible light absorption of the ZIF-67 [161]. Direct sulfurization of ZnO@ZIF composite was approached to acquire ZnO@ZnS, ZnO@CoS, and ZnO@ZnS/CoS heterostructured. The prepared heterostructures were investigated for their PEC activity, and ZnO@ZnS/CoS heterostructure exhibited the highest photocurrent density of 2.46 $mAcm^{-2}$ with a photoconversion efficiency of 0.65%. The enchanced PEC activity is due to the special cellular structure, which increases the number of active sites and long incident photon transport pathway [162]. The hydrothermal method was used to prepare zeolite-type chalcogenide CPM-121 integrated with TiO_2 nanowires. The PEC investigation of the prepared heterostructure showed a 3 fold increase in the photocurrent under visible light irradiation. The increase in the photocurrent is due to the formation of heterostructure, which facilitates electron transport [163].

7. 2D Materials For PEC Water Splitting

Graphene oxide is a 2-dimensional material that has gained attention for its unique properties for PEC water splitting [164]. The solvothermal method was used to prepare a sulfur-doped titanium oxide on the surface of sulfur-doped reduced graphene oxide (rGO) nanocomposite. The photocurrent density exhibited by the S-TiO_2/S-rGO was 3.36 mA/cm^2, which was 3 times higher than the bare TiO_2. The enhanced PEC performance of S-TiO_2/S-rGO is due to efficient visible light harvesting and reduced recombination rate of photogenerated hole and electron pair. It was studied from the HR-TEM image that a strong coupling was seen between S-TiO_2 and S-RGO, which during the PEC water splitting process enabled the transfer of electrons from S-TiO_2 to S-rGO [165]. The hydrothermal process synthesized a graphene oxide/ZnO hybrid structure. The prepared hybrid material showed a photocurrent density of about 1.517 mA/cm^{-2}. This enhanced PEC performance is due to the increased oxygen vacancies from the formation of graphene oxide/ZnO hybrid [166]. The wet impregnation method was used to prepare Mo-$BiVO_4$@rGO [167]. The SEM image showed the porous sheet structure of rGO in which the $BiVO_4$ particle was embedded. The prepared material showed a hydrogen conversion efficiency of 2.45% at 0.6 V versus RHE, which was higher than the $BiVO_4$ [167]. To investigate the hydrogen evolution further, the water-splitting reactions at zero potential were performed using the Xenon lamp and aqueous solutions of 1M Na_2S and 1M Na_2SO_3. Figure 14 shows a comparison of the hydrogen generation yield obtained for pure $BiVO_4$, Mo-$BiVO_4$, and Mo-$BiVO_4$@rGO nanocomposite after three hours of the experiment. Among all examined materials, the Mo-$BiVO_4$@rGO nanocomposite exhibited the highest rate of hydrogen evolution. The enhanced PEC performance resulted from the improved charge carrier density, enhanced electronic conductivity from the doping of Mo, and increased carrier transport and collection efficiency due to rGO.

Hexagonal boron nitride has a wide bandgap of 5.2 eV. It has gained considerable attention due to its unique properties like high chemical stability and thermal conductivity. It was depicted in recent studies that it shows a semiconducting and electronic transport similar to that of metals and metal oxide [168,169]. Calcium copper titanium with different amounts of exfoliated hexagonal boron nitride was prepared through a solid-state reaction method. The prepared material showed an enhanced photocurrent generation, which was 16 times higher than the pure material. The enhancement in the activity is due to the formation of new bonds after the insertion of B and N elements and the generated oxygen vacancy. It was seen from the SEM image that the grain boundary thickness increased and the grain size reduced, which is due to the increase in the amount of CuO phase after adding the nanosheet [170]. A low-temperature plasma-enhanced chemical vapor deposition method was used to prepare a vertically aligned carbon-doped boron nitride on a conductive substrate. The carbon-doped boron nitride showed a photocurrent density of 120 μA cm^{-2} which was 60 times higher than the carbon-doped boron nitride achieved by the traditional deposition method. The enhanced PEC activity is due to the doping of carbon; it was observed that as the content of carbon increased, there was an increase in visible light absorption. The TEM image showed a separated nanofilm of carbon-doped boron nitrite, and highly ordered layered structures were observed in the HR-TEM image. Few additional peaks were observed in the UV spectra, which indicates a minor increase in the light absorption in the visible light [171]. The solvothermal method was used to prepare CdSe quantum dots coupled with different weight percent of ultra-thin layered hexagonal porous boron nitride sheets functionalized with 3-

mercaptopropionic acid. The prepared heterostructure showed an H_2 evolution of 25 128 μmol g^{-1} h^{-1}. The performance of the prepared heterostructure was 18.6 times higher than functionalized boron nitride sheets. The enhanced performance is due to the high specific area of the boron nitride sheet, which allows the uniform deposition of the quantum dots, increasing the absorption sites and the thiol group of 3-mercaptopropionic acid strongly tethers the quantum dots to the nanosheet. Such a high specific area reduces the recombination of photogenerated charge carriers, electrons, and holes. The heterostructure showed a photocurrent density of 1.2 mA cm_{-2} at 1.2 V vs. Ag/AgCl, and it was 4.13 and 2.56 times higher than pure boron nitride and CdSe quantum dots, respectively. The deposition of CdSe quantum dots on the nanosheet was seen in the TEM image [172].

Graphitic carbon nitrite ($g\text{-}C_3N_4$) has gained attention as a photoanode material due to its unique properties like tunable electronic structure and visible absorption range. They are non-toxic, cheap, and exhibit high physicochemical stability while requiring a simple fabrication route [173,174]. The disadvantage of this material is that it tends to have a high recombination rate of photogenerated electron and hole pair, poor electronic conductivity, slow hole transfer, and limited visible light absorption range of 460 to 760 nm [175,176]. These materials have studied for various application like photoelectronic devices [177], PEC biosensing [178], electrochemiluminescence [179], photocurrent generation [180]. Karjule et al. have shown PEC properties, electropolymerization ability, and photoswitching properties of polycyclic aromatic hydrocarbons as a base for new photoelectronic devices. Yang et al. have tailored C atoms in graphene, forming an intriguing electronic structure leading to efficient photoelectron interconversion. PEC activities and excellent biocompatibility of the carbon nitrides help analyze non-transparent biosamples, creating a versatile platform for diagnosing various diseases [178]. Zhao et al. developed carbon nitrides-based electrodes for boosting photocurrent and electrochemiluminescence. They claimed that the cathodic efficiency of electrochemiluminescence reached 7 times as compared to Ru(bpy)$_3$Cl$_2$ in an aqueous solution [179]. Zhang et al. have synthesized polymeric g-C_3N_4, which shows a photovoltaic effect and, as a photoactive material, produces electricity from solar light [180]. The template-free hydrothermal method was used to prepare the SnO_2-g-C_3N_4 nanostructure. The prepared nanostructure showed 8 times higher PEC performance compared to pure SnO_2. The enhanced PEC performance is due to the improved charge separation of photogenerated electron and hole pairs and improved visible light absorption. The formation of heterojunction between SnO_2 and g-C_3N_4 improved the charge separation of electron and hole, improving the PEC performance of the heterostructure. The UV spectra depicted that the SnO_2-g-C_3N_4 showed an absorption edge in between SnO_2 and g-C_3N_4 and much closer to g-C_3N_4. It was observed that the absorption intensity increased in the visible light region after the addition of SnO_2 [181]. Vanadium doped g-C_3N_4 was prepared by direct calcination of urea and ammonium metavanadate. The vanadium doped g-C_3N_4 showed a photocurrent density of 0.80 mA cm^{-2}, which is 40 times higher than pure g-C_3N_4. The improvement in the PEC performance is due to the prolonged light absorption, improved transfer of electrons and holes, and extra active catalytic sites. A densely crumpled nanosheet structure was seen for vanadium-doped g-C_3N_4 under TEM. The EDAX mapping of vanadium doped g-C_3N_4 showed the presence of C, N, and V. It shows that the vanadium is evenly distributed. The UV spectra of the vanadium doped g-C_3N_4 showed that the optical band gap decreased with an increase in V concentration. The decrease in the optical band gap indicated the improvement in the charge mobility and light absorption, which improves the PEC performance [182].

Transition metal dichalcogenides is a 2-dimensional material with a MeX_2 structure where Me is a transition metal atom-like Mo, W, etc. and X is a chalcogenide atom-like S, Se, or Te [119,183]. The Me atom is sandwiched between two X atom layers and bonds to other layers by weak van deer Waals's interaction. These materials can easily be exfoliated to a few single layers and have high conductivity, strength, and stability [184,185]. These materials have been studied for various applications such as photovoltaics, organic light-emitting diodes, transistor, photodetectors, and gas sensors [186,187].

Molybdenum disulfide (MoS_2) is a 2-dimensional transition metal chalcogenide and has gained considerable attention for various applications due to its mechanical, electrical, and optical properties [188]. Ag embedded MoS_2/$BiVO_4$ was prepared through an electrophoretic deposition method on an FTO glass substrate. The prepared heterostructure showed a photocurrent density of 2.72 mA cm^{-2}, which is 2.44 times higher than pure material. The enhanced PEC performance is due to the formation of heterostructure between MoS_2 and $BiVO_4$, delaying the recombination of electron-hole pairs. The formation of Ag embedded MoS_2/$BiVO_4$ was confirmed from the TEM image. The sharp peak on the XRD pattern indicates the formation of a nanoporous monoclinic scheelite structure [189]. TiO_2 nanotube arrays (TNAs) were prepared by the anodization method, and MoS_2 was prepared by the hydrothermal method. The MoS_2@PVA/TNA was prepared by coating MoS_2 dispersed in PVA solution. The prepared material showed a photocurrent of 65 $\mu A/cm^2$ at 0 V vs. Ag/AgCl. The enhanced PEC activity is due to the formation of type II heterostructure, which promotes the migration of electrons and holes under excitation. The XRD spectra confirmed the formation of MoS_2@PVA/TNA [190]. ZnO/MoS2 nano cable arrays were prepared on an FTO glass through the solvothermal method and showed an improved photocurrent of 1.39 mA cm^{-2} compared to the pure materials. The enhancement in the PEC performance is due to the expanded light-harvesting capability and fast charge separation and transport through the nano cable structure. The TEM image conformed to the formation of the ZnO/MoS_2 nano cable. In the UV spectra, it was observed that the ZnO/MoS_2 showed a redshift, indicating an expanded absorption [191].

Tungsten disulfide (WS_2) is a 2-dimensional material whose electrical and optoelectronic properties can be tuned by molding the number of layers and crystal cites. It has a high specific area, leading to the presence of high active sites. It is non-toxic, inexpensive, and resistant to corrosion, which makes it a suitable material for PEC water splitting. The disadvantage of this material is that it has a high recombination rate of photogenerated electron and hole pair and low charge transfer efficiency [192–195]. WS_2 nanosheet doped with Ti and Mo was prepared at a relatively low temperature through the CVD process. WS_2 nanosheet doped with both Ti and Mo showed increased PEC performance, while Ti-doped WS_2 nanosheet exhibiting the highest photocurrent density of 10.44 mA/cm^2. Ti-doped WS_2 showed a charge transfer resistance of 6.3 kΩ which was two times less than pure WS_2 nanosheets. This enhancement in the PEC performance is due to the increase in the donor density and improvement in the electrical conductivity. The FESEM image confirmed the doping of Ti and Mo in the WS_2 nanosheet. The concentration of atoms calculated from the EDS spectrum also confirmed that Ti and Mo were doped in the WS_2 nanosheet. The DRS spectra showed bandgap reduction after doping Ti and Mo, indicating an increase in the light absorption, which will improve the PEC performance [196]. WS_2 nanosheet was prepared by liquid-phase exfoliation by ultrasonication. WO_3 was prepared by ultrasonication followed by calcination. WO_3/WS_2 photoanode was prepared by the dropping casting method. It was seen that the photocurrent density of the WO_3/WS_2 photoanode increased considerably. It showed a photocurrent density of 5.6 $mAcm^{-2}$, which was 7.2 times higher than the pure material. The enhancement in the photocurrent density is due to the increase in the donor concentration, reduced space charge layer, and decreased flat band potential. The SEM and TEM images confirmed the formation of a 2-dimensional plate-like structure of WO_3/WS_2 photoanode [197].

8. Molecular dynamics for water splitting

Molecular dynamics (MD) is a powerful computational tool for simulating and evaluating the dynamics of molecular systems. Newtonian laws of motion are the main principle of molecular dynamics. The statistical ensembles of MD usually control the number of particles, temperature, and pressure. A sequence of methods is followed to define the global MD algorithm, such as parameters of force field must be inserted, update configuration algorithm, and post-processing [198]. PEC depends on catalyzed charge transfer reactions at solid-liquid interfaces. The charge transfer process, formed products, and the distribution of electronic charge carriers and ions play a vital role in the evaluation of the PEC system. The performance of PEC can be optimized by knowing the transport of ionic species within the liquid bulk phase. The evaluation of PEC and reactions by numerical aspects in the water splitting applications can be simplified by MD. Quantum chemical ab initio-based MD models help to inspect chemical surface processes during water splitting. The alignment of the valence and conduction band edges to the water redox potential can provide insight into the properties of semiconductor materials used for water splitting applications. Zunger et al. have given some approaches to understanding interfacial reaction and vacuum calculations [199]. Cheng et al. showed the alignment of the conduction band edge with the normal hydrogen electrode quite similar to the experimental value [200]. The vital role of surface adsorbates in the position of conduction and valence band edges was investigated by Zhou et al. using DFT MD approaches [201]. Molecular dynamics simulation was used to quantify water dissociation over the TiO2 surfaces at various water coverages. The extent of water dissociation predicted by the ReaxFF reactive force field was in general agreement with previous density-functional theory studies and experiments [202]. Here, they have simulated the potential-dependent OH and O adsorption on Pt(111) and Pt_3Ni. The simulations are performed employing DFT calculated interaction and formation energies as input to Monte Carlo simulations [203].

9. Perspective and conclusions

The application of PEC water splitting is the eco-friendly route for hydrogen production. Hydrogen is one of the most abundant materials seen in almost 95% of the visible matter on earth while being the lightest and smallest element. It exhibits some unique properties which act as a benefit and a challenge to use hydrogen as a fuel. It is odorless, invisible, nontoxic, noncarcinogenic, nonpoisonous, smoke-free, and highly buoyant [204–206]. Hydrogen tends to combine with other elements like carbon and oxygen, and it is naturally on the earth's crust in a very small amount. Hydrogen showed unique properties like high diffusivity, low viscosity, inimitable chemical nature, combustibility, and electrochemical properties that make it a better fuel. A hydrogen is a form of alternative, non-conventional or advanced categories of fuel [207–209]. Hydrogen has a high heating value compared to other fuels [2, 3].

Hydrogen can be sorted, and the storage of hydrogen is one of the most important technologies needed for the long-term use of hydrogen. Hydrogen from the salt caverns can be used on a cloudy day when the solar and wind are not active [210–212]. The liquid form of storage of hydrogen is in the form of cryogenic liquid. The density of the liquid to be stored is too high, 71 g/L, and has a boiling point of 20 K. To store hydrogen, special double-walled vessels with a good insulation system are needed to prevent heat leakage [213–215]. In a solid-state system, hydrogen is stored in physisorption or chemisorption. In physisorption, carbon-based materials such as carbon nanotubes, fibers, fullerenes, activated carbon, zeolites, metal-organic framework, covalent organic framework, and polymers of intrinsic microporosity are used to absorb molecular hydrogen on the surface by van der Waals force. The few drawbacks of this system are that they have low hydrogen storage capacity and require extremely low temperature for high hydrogen storage. In chemisorption, the hydrogen atom chemically reacts to the solids to form hydrides. These chemical hydrides can release hydrogen under relatively moderate operating conditions [216,217].

PEC water splitting is a clean source for producing hydrogen. Many possible factors affecting the water splitting are being highlighted in this review. Multifunctional materials with superior properties such as perovskites, semiconductor oxides, carbon materials, metal-organic frameworks, and 2D materials have immense potential to enhance PEC water splitting, generating a clean and renewable energy source. Table 1 shows various materials, their light source, current density, and electrolyte for PEC water splitting. PEC systems need to be progressed at a commercialized industrial level device in the near future to produce valuable fuels to develop a sustainable economy. Many processes such as photocatalysis, PEC catalysis, and photovoltaic-driven electrocatalysis are employed to optimize the performance of these systems. Mainly to progress the usage of PEC in the industrial sector, more understandings of the working mechanisms, prototype design, enhancing the current density, measurement capabilities, exploration of new efficient materials, and durable interfaces. Looking deeply into the above parameters, at first the facility needs to get ready to test the prototype and component performance, which is of broad interest to customers showing them peak efficiency, spectral response, and stability. This approach can attract investor attention to industry efforts in designing efficient prototypes of PEC. Secondly, the industry needs to set up test beds for PEC systems with access to adequate light replicating solar illumination, gas outlets linked to flowmeters, and a gas chromatography device. A device's performance can be evaluated by knowing solar-to-fuel efficiency, degradation rate, faradic efficiency, and spectral response. Thirdly, at the industrial level, distinguishing and reducing artifacts (chemical corrosion, calibration of light and photodiode, various illumination devices) in PEC systems is vital to improve performance. Hence best practices in design and investigation can lead to desired results in improving the efficiency of PEC in the industrial sector.

Exploration of new efficient materials for PEC bearing superior electro-optical properties can ensure high-efficiency energy conversion. Some computational techniques such as kinetic growth simulations and density functional theory may help shed light on interfacial reactions, vapor-phase synthesis optimization, and nucleation. Moreover, large-area handling of high-performance materials needs to be developed to extend the use of the PEC in industries. Some of the important considerations also need to be focused upon is the corrosion of the active material in the electrolyte environment. Industrial level measurement capabilities such as overlayer technology or surface passivation can help to reduce such decay in performance. These focus on the perspective of utilizing lab-scale PEC into efficient industrial systems for efficient fuel generation.

The hydrogen generation from the water splitting was discussed in this paper considering the electrolytic, thermochemical, mechanocatalytic, plasmolytic, photocatalytic, and PEC methods. Despite the plenty of these technologies, many still encounter serious problems. For instance, one of the major challenges of photocatalytic and photoelectrocatalytic systems is to find an appropriate material that absorbs solar radiation in a broad range of wavelengths. Furthermore, a catalyst should have suitable band edge positions and exhibit a high yield of photogenerated carrier separation. The stability of the catalyst and its cost of its are also important factors that determine the range of its possible applications. Till now, the different approaches have been recognized as promising for overcoming the challenges listed above. An interesting strategy for increasing the water splitting efficiency is the development of binary materials, in which morphologies and surface compositions can be tuned in a facile way. Furthermore, semiconductor heterojunctions can improve charge transfer and reduce the recombination of photogenerated electron-hole pairs. Similar effects can be obtained through doping the semiconductor that changes the local electronic structure of the material and enriches the accessible catalytic active sites. Further studies in PEC hydrogen evolution should focus on combining the various catalytic materials into metal-organic frameworks or binary and even ternary nanocomposites. The specific surface area of the catalyst plays a key role in exposing the active sites and reducing the path for mass and charge transport. Therefore, new structural engineering strategies have been developed to design and fabricate efficient catalysts with cutting-edge morphologies, including aligned nanorods, nanocavity arrays, nanotube hollow structures, interwoven nanosheets, nanoflowers formed by the nanoflakes stacking, and nanoparticles encapsulated into the nanosheets. It is expected that future improvement of stability of the materials reviewed and optimization of costs of their production will result in large-scale industrial production of the hydrogen.

Acknowledgment:

This study is supported by Basic Science Research Program through the National Research Foundation of Korea (NRF), funded by the Ministry of Science and ICT of Korea (2021R1C1C1011588). KM like to thank the Silesian University of Technology (Gliwice, Poland) through the Rector's pro-quality grant (14/010/RGJ21/0006) and Rector's habilitation grant (14/010/RGH21/0008) in the area of scientific research and development. This study was also supported by the JST-ERATO Yamauchi Materials Space-Tectonics Project (Grant Number: JPMJER2003). This work was performed in part at the Queensland node of the Australian National Fabrication Facility, a company established under the National Collaborative Research Infrastructure Strategy to provide nano and microfabrication facilities for Australia's researchers.

References

[1] T.N. Veziroğlu, S. Şahin, Energy Convers. Manag. 49 (2008) 1820–1831.

[2] T. Nejat Veziroglu, Energy Procedia 29 (2012) 654–656.

[3] I. Iordache, A. V. Gheorghe, M. Iordache, Int. J. Hydrogen Energy 38 (2013) 12231–12240.

[4] X. Luo, J. Wang, M. Dooner, J. Clarke, Appl. Energy 137 (2014) 511-536.

[5] P. Mary Rajaitha, K. Shamsa, C. Murugan, K.B. Bhojanaa, S. Ravichandran, K. Jothivenkatachalam, A. Pandikumar, SN Appl. Sci. 2 (2020) 572.

[6] F. Mueller-langer, E. Tzimas, M. Kaltschmitt, S. Peteves, International Journal of Hydrogen Energy 32 (2007) 3797–3810.

[7] G. Marbán, T. Valdés-Solís, Int. J. Hydrogen Energy 32 (2007) 1625–1637.

[8] A. Midilli, M. Ay, I. Dincer, M.A. Rosen, Renewable and Sustainable Energy Reviews 9 (2005) 255–271.

[9] Y. Guo, J. Tang, Z. Wang, Y. Sugahara, Y. Yamauchi, Small 14 (2018) 1802442.

[10] P. Bhanja, Y. Kim, B. Paul, T. Debnath, J. Lin, Chem. Eng. J. 396 (2020) 125245.

[11] V. Veeramani, B.M. Matsagar, Y. Yamauchi, A. Yacine, M. Naushad, M. Habila, S. Wabaidur, Z.A. Alothman, Z. Wang, K.C. Wu, J. Taiwan Inst. Chem. Eng. 96 (2019) 634–638.

[12] B. Sørensen, Energy Policy 19 (1991) 386–391.

[13] I. Dincer, C. Acar, Int. J. Hydrogen Energy 40 (2014) 11094–11111.

[14] B You, Y Sun, Acc. Chem. Res. 51 (2018) 1571–1580

[15] L.G. Bloor, P.I. Molina, M.D. Symes, L. Cronin, J. Am. Chem. Soc. 136 (2014) 3304–3311.

[16] X. Shang, J. Qin, J. Lin, B. Dong, J. Chi, Z. Liu, L. Wang, Y. Chai, C. Liu, J. Colloid Interface Sci. 523 (2018) 121–132.

[17] J. Wang, L. Ji, X. Teng, Y. Liu, L. Guo, Z. Chen, J. Mater. Chem. A 7 (2019) 13149–13153.

[18] B. Rausch, M.D. Symes, L. Cronin, J. Am. Chem. Soc. 135 (2013) 13656–13659.

[19] M.D. Symes, L. Cronin, Nat Chem. 5 (2013) 403-409.

[20] M. Carmo, D.L. Fritz, J. Mergel, D. Stolten, Int. J. Hydrogen Energy 38 (2013) 4901–4934.

[21] M. Schalenbach, M. Carmo, D.L. Fritz, International Journal of Hydrogen Energy 8 (2013) 14921-14933.

[22] S.A. Grigoriev, V.I. Porembsky, V.N. Fateev, Int. J. Hydrogen Energy 31 (2006) 171–175.

[23] P. Millet, R. Ngameni, S.A. Grigoriev, N. Mbemba, F. Brisset, A. Ranjbari, International Journal of Hydrogen Energy 35 (2010) 5043–5052.

[24] B. Liu, C. Wang, Y. Chen, Electrochimica Acta 264 (2018) 350–357.

[25] S.S. Kumar, S.U.B. Ramakrishna, B.R. Devi, V. Himabindu, SAJ of Chemical Engineering 25 (2018) 1.

[26] W. Xu, K. Scott, Int. J. Hydrogen Energy 35 (2010) 12029–12037.

[27] S.S. Kumar, V. Himabindu, Mater. Sci. Energy Technol. 2 (2019) 442–454.

[28] A. Ursua, L.M. Gandia, P. Sanchis, Proc. IEEE 100 (2012) 410–426.

[29] S. Seetharaman, R. Balaji, K. Ramya, K.S. Dhathathreyan, Int. J. Hydrogen Energy 38 (2013) 14934–14942.

[30] D. Burnat, M. Schlupp, A. Wichser, B. Lothenbach, M. Gorbar, A. Züttel, U.F. Vogt, J. Power Sources 291 (2015) 163–172.

[31] S. Marini, P. Salvi, P. Nelli, R. Pesenti, M. Villa, M. Berrettoni, G. Zangari, Y. Kiros, Electrochim. Acta 82 (2012) 384–391.

[32] K. Zeng, D. Zhang, Prog. Energy Combust. Sci. 36 (2010) 307–326.

[33] V. Marinović, A.R. Despić, Electrochim. Acta 44 (1999) 4073–4077.

[34] L. De Silva Muñoz, A. Bergel, D. Féron, R. Basséguy, Int. J. Hydrogen Energy 35 (2010) 8561–8568.

[35] W. Dönitz, E. Erdle, Int. J. Hydrogen Energy 10 (1985) 291–295.

[36] L. Bi, S.P. Shafi, E. Traversa, J. Mater. Chem. A 3 (2015) 5815–5819.

[37] M.A. Laguna-Bercero, J. Power Sources 203 (2012) 4–16.

[38] X. Yue, A. Yan, M. Zhang, L. Liu, Y. Dong, M. Cheng, 185 (2008) 691–697.

[39] M. Ni, M.K.H.L. Ã, D.Y.C. Leung, Int. J. of Hydrogen Energy 33 (2008) 2337–2354.

[40] P. Moçoteguy, A. Brisse, Int. J. Hydrogen Energy 38 (2013) 15887–15902.

[41] A. T-Raissi, Encycl. Inorg. Bioinorg. Chem. (2011) 1–9.

[42] F. Safari, I. Dincer, Energy Convers. Manag. 205 (2020) 112182.

[43] J. E. Funk, Int. J. Hydrogen Energy 26 (2001) 185–190.

[44] G. Naterer, S. Suppiah, M. Lewis, K. Gabriel, I. Dincer, M.A. Rosen, M. Fowler, G. Rizvi, E.B. Easton, B.M. Ikeda, M.H. Kaye, L. Lu, I. Pioro, P. Spekkens, P. Tremaine, J. Mostaghimi, J. Avsec, J. Jiang, Int. J. Hydrogen Energy 34 (2009) 2901–2917.

[45] F.J. Navas, R. Alcántara, C. Fernández-Lorenzo, J. Martín, Rev. Sci. Instrum. 80 (2009) 063102.

[46] B. Bulfin, J. Vieten, C. Agrafiotis, M. Roeb, C. Sattler, J. Mater. Chem. A 5 (2017) 18951–18966.

[47] C. Jarrett, W. Chueh, C. Yuan, Y. Kawajiri, K.H. Sandhage, A. Henry, Sol. Energy 123 (2016) 57–73.

[48] X. Vitart, A. Le Duigou, P. Carles, Energy Convers. Manag. 47 (2006) 2740–2747.

[49] G. Cerri, C. Salvini, C. Corgnale, A. Giovannelli, D. De Lorenzo Manzano, A.O. Martinez, A. Le Duigou, J.M. Borgard, C. Mansilla, Int. J. Hydrogen Energy 35 (2010) 4002–4014.

[50] J.H. Norman, K.J. Mysels, R. Sharp, D. Williamson, Int. J. Hydrogen Energy 7 (1982) 545–556.

[51] H. Ishaq, I. Dincer, G.F. Naterer, Energy Convers. Manag. 171 (2018) 384–397.

[52] Y.H. Jeong, M.S. Kazimi, Nucelear Technology, 159 (2017) 147-157.

[53] S. Ikeda, T. Takata, T. Kondo, G. Hitoki, M. Hara, J.N. Kondo, K. Domen, H. Hosono, H. Kawazoe, A. Tanaka, Chem. Commun. 2 (1998) 2185–2186.

[54] M. Hara, M. Komoda, H. Hasei, M. Yashima, S. Ikeda, T. Takata, J.N. Kondo, K. Domen, J. Phys. Chem. B 104 (2000) 780–785.

[55] T. Ohta, Int. J. Hydrogen Energy 26 (2001) 401.

[56] V. GIVOTOV, A. FRIDMAN, M. KROTOV, E. KRASHENINNIKOV, B. PATRUSHEV, V. RUSANOV, G. SHOLIN, Int. J. Hydrogen Energy 6 (1981) 441–449.

[57] X. Chen, S.L. Suib, Y. Hayashi, H. Matsumoto, J. Catal. 201 (2001) 198–205.

[58] K. Fujishima, A., & Honda, Nature 238 (1972) 37–38.

[59] H. Lv, Y. V Geletii, C. Zhao, J.W. Vickers, G. Zhu, C.L. Hill, Chem. Soc. Rev.41 (2012) 7572–7589.

[60] Z. Han, R. Eisenberg, Acc. Chem. Res. 47 (2014) 2537–2544.

[61] Z. Wang, C Li, K Domen, Chem. Soc. Rev. 48 (2019) 2109–2125.

[62] K. Maeda, "Journal Photochem. Photobiol. C Photochem. Rev. 12 (2011) 237–268.

[63] S. Berardi, S. Drouet, L. Franca, C. Gimbert-surin, M. Guttentag, C. Richmond, T. Stoll, A. Llobet, Chem. Soc. Rev. (2014) 7501–7519.

[64] L. Jiao, Y. Dong, X. Xin, L. Qin, H. Lv, Appl. Catal. B Environ. 291 (2021) 120091.

[65] M. Zhang, H. Li, J. Zhang, H. Lv, G.Y. Yang, Chinese J. Catal. 42 (2021) 855–871.

[66] K. Maeda, K. Domen, The J. of Phy Chem C 111 (2007) 7851–7861.

[67] F.E. Osterloh, B.A. Parkinson, G. Editors, MRS bulletin 36 (2011) 17–22.

[68] K. Rajeshwar, Reviews in Applied Electrochemistry 37 (2007) 765–787.

[69] A. Kudo, Y. Miseki, Chem. Soc. Rev. 38 (2009) 253–278.

[70] W. Yang, R.R. Prabhakar, J. Tan, S.D. Tilley, J. Moon, Chem. Soc. Rev. 48 (2019) 4979–5015.

[71] S. Vinoth, P.M. Rajaitha, A. Pandikumar, New J. Chem. 45 (2021) 2010–2018.

[72] M.D. Stoller, S. Park, Y. Zhu, J. An, R.S. Ruoff, Nano Lett. 8 (2008) 3498–3502.

[73] K. Glanz, Int. J. Hydrogen Energy 27 (2010) 991–1022.

[74] X. Li, Z. Xin, S. Xia, X. Gao, C. Tung, L. Wu, Chem. Soc. Rev. (2020) 9028–9056.

[75] H. Lv, C. Wang, G. Li, R. Burke, T.D. Krauss, Y. Gao, R. Eisenberg, Proc. Natl. Acad. Sci. USA (2017) 114, 11297-11302.

[76] H. Wu, X. Li, Y. Wang, S. Zhou, Y. Chen, X. He, C. Tung, L. Wu, J. Mater. Chem. A (2019) 26098–26104.

[77] J. Zhang, M. Zhang, Y. Dong, C. Bai, Y. Feng, L. Jiao, H. Lv, Nano Res. 15 (2022) 1347–1354.

[78] M. Ni, M.K.H.L. Ã, D.Y.C. Leung, K. Sumathy, Renewable and Sustainable Energy Reviews 11 (2007) 401–425.

[79] J. Nowotny, C.C. Sorrell, L.R. Sheppard, T. Bak, Int. J. Hydrogen Energy 30 (2005) 521–544.

[80] I. Cesar, A. Kay, J.A. Gonzalez Martinez, M. Grätzel, J. Am. Chem. Soc. 128 (2006) 4582–4583.

[81] L. Clarizia, D. Spasiano, I. Di Somma, R. Marotta, R. Andreozzi, D.D. Dionysiou, Int. J. Hydrogen Energy 39 (2014) 16812–16831.

[82] R. Abe, J. Photochem. Photobiol. C Photochem. Rev. 11 (2010) 179–209.

[83] Y. Xu, R. Xu, Appl. Surf. Sci. 351 (2015) 779–793.

[84] J. Wen, J. Xie, X. Chen, X. Li, Appl. Surf. Sci. 391 (2017) 72–123.

[85] V. Etacheri, C. Di Valentin, J. Schneider, D. Bahnemann, S.C. Pillai, J. Photochem. Photobiol. C Photochem. Rev. 25 (2015) 1–29.

[86] K.P.S. Parmar, H.J. Kang, A. Bist, P. Dua, J.S. Jang, J.S. Lee, ChemSusChem 5 (2012) 1926–1934.

[87] J.H. Kim, Y. Jo, J.H. Kim, J.W. Jang, H.J. Kang, Y.H. Lee, D.S. Kim, Y. Jun, J.S. Lee, ACS Nano 9 (2015) 11820–11829.

[88] T.W. Kim, Y. Ping, G.A. Galli, K. Choi, Nat. Commun. 6 (2015) 8769.

[89] J. Wang, C. Du, Q. Peng, J. Yang, Y. Wen, B. Shan, R. Chen, Int. J. Hydrogen Energy (2017) 1–10.

[90] S.S. Kalanur, I.H. Yoo, K. Eom, H. Seo, J. Catal. 357 (2018) 127–137.

[91] W. Zhang, M. Liu, ACS Energy Lett. 4 (2019) 834–843.

[92] W. Yang, J. Ahn, Y. Oh, J. Tan, H. Lee, J. Park, H. Kwon, J. Kim, W. Jo, J. Kim, J. Moon, Adv. Energy Materials 8 (2018) 1702888.

[93] Y. Li, T. Takata, D. Cha, K. Takanabe, T. Minegishi, J. Kubota, K. Domen, Adv. Mater. 25 (2013) 125–131.

[94] E. Environ, J. Oh, T.G. Deutsch, H. Yuan, H.M. Branz, (2011) 1690–1694.

[95] H. Kumagai, T. Minegishi, N. Sato, T. Yamada, J. Kubota, K. Domen, J. Mater. Chem. A 3 (2015) 8300–8307.

[96] F. Le Formal, N. Tétreault, M. Cornuz, T. Moehl, M. Grätzel, K. Sivula, Chem. Sci. 2 (2011) 737–743.

[97] Y.S. Lee, D. Chua, R.E. Brandt, S.C. Siah, J. V. Li, J.P. Mailoa, S.W. Lee, R.G. Gordon, T. Buonassisi, Adv. Mater. 26 (2014) 4704–4710.

[98] M. Baek, M. Zafar, S. Kim, D.H. Kim, C.W. Jeon, J. Lee, K. Yong, ChemSusChem 11 (2018) 3679–3688.

[99] H. Kim, H. Bae, S.W. Bang, S. Kim, S.H. Lee, S.-W. Ryu, J.-S. Ha, Opt. Express 27 (2019) A206-A215.

[100] D.K. Lee, K.S. Choi, Nat. Energy 3 (2018) 53–60.

[101] E. Hussain, I. Majeed, M.A. Nadaem, A. Badshah, Y. Chen, M.A. Nadeem, R. Jin, J. Phys. Chem. C 120 (2016) 17205–17213.

[102] W. Zhu, X. Liu, H. Liu, D. Tong, J. Yang, J. Peng, J. Am. Chem. Soc. 132 (2010) 12619–12626.

[103] Y.C. Pu, G. Wang, K. Der Chang, Y. Ling, Y.K. Lin, B.C. Fitzmorris, C.M. Liu, X. Lu, Y. Tong, J.Z. Zhang, Y.J. Hsu, Y. Li, Nano Lett. 13 (2013) 3817–3823.

[104] G.K. Mor, O.K. Varghese, M. Paulose, K. Shankar, C.A. Grimes, Sol. Energy Mater. Sol. Cells 90 (2006) 2011–2075.

[105] M. Hamadanian, A. Reisi-Vanani, A. Majedi, Appl. Surf. Sci. 256 (2010) 1837–1844.

[106] Z. Dong, D. Ding, T. Li, C. Ning, Appl. Surf. Sci. 443 (2018) 321–328.

[107] Z. Li, L. Shi, D. Franklin, S. Koul, A. Kushima, Y. Yang, Nano Energy 51 (2018) 400–407.

[108] C. Di Valentin, G. Pacchioni, Acc. Chem. Res. 47 (2014) 3233–3241.

[109] W. Li, P. Da, Y. Zhang, Y. Wang, X. Lin, X. Gong, G. Zheng, ACS Nano 8 (2014) 11770–11777.

[110] S.S. Kalanur, Catalysts 9 (2019) 456.

[111] S.S. Kalanur, H. Seo, J. Colloid Interface Sci. 509 (2018) 440–447.

[112] A. Paracchino, Nat. Mater. 10 (2011) 456–461.

[113] T. Wang, Y. Wei, X. Chang, C. Li, A. Li, S. Liu, J. Zhang, J. Gong, Appl. Catal. B Environ. 226 (2018) 31–37.

[114] L. Pan, J.H. Kim, M.T. Mayer, M. Son, A. Ummadisingu, J.S. Lee, A. Hagfeldt, J. Luo, M. Grätzel, Nat Catalysis 1 (2018) 412-420.

[115] S. Zhang, J. Yan, S. Yang, Y. Xu, X. Cai, X. Li, X. Zhang, F. Peng, Y. Fang, Chinese J. Catal. 38 (2017) 365–371.

[116] Q. Ma, J.P. Hofmann, A. Litke, E.J.M. Hensen, Solar Energy Materials and Solar Cells 141 (2015) 178–186.

[117] Y.K. Hsu, C.H. Yu, Y.C. Chen, Y.G. Lin, Electrochim. Acta 105 (2013) 62–68.

[118] E.M. Kaidashev, M. Lorenz, H. Von Wenckstern, A. Rahm, H.C. Semmelhack, K.H. Han, G. Benndorf, C. Bundesmann, H. Hochmuth, M. Grundmann, Appl. Phys. Lett. 82 (2003) 3901–3903.

[119] M. Xu, T. Liang, M. Shi, H. Chen, Chem. Rev. 113 (2013) 3766–3798.

[120] D. Chaudhary, S. Singh, V.D. Vankar, N. Khare, J. Photochem. Photobiol. A Chem. 351 (2018) 154–161.

[121] M. Wu, W. Chen, Y. Shen, F. Huang, C.-H. Li, S. Li, ACS Appl. Mater. Interfaces 6 (2014) 15052–15060.

[122] R. Wei, P. Kuang, H. Cheng, Y. Chen, J. Long, M. Zhang, Z. Liu, J., ACS Sustainable 5 (2017) 4249-4257.

[123] R. Van De Krol, Y. Liang, J. Schoonman, (2008) 2311–2320.

[124] F. Le Formal, M. Grätzel, K. Sivula, Adv. Funct. Mater. 20 (2010) 1099–1107.

[125] A.A. Tahir, K.G.U. Wijayantha, S. Saremi-Yarahmadi, M. Mazhar, V. McKee, Chem. Mater. 21 (2009) 3763–3772.

[126] A.G. Joly, J.R. Williams, S.A. Chambers, G. Xiong, W.P. Hess, D.M. Laman, J. Appl. Phys. 99 (2006) 10.1063/1.2177426.

[127] X. Yu, J. Liu, W. Yin, T. Wang, L. Quan, Y. Ran, J. Cui, L. Wang, Y. Zhang, Appl. Surf. Sci. 492 (2019) 264–271.

[128] N.A. Arzaee, M.F. Mohamad Noh, A. Ab Halim, M.A.F. Abdul Rahim, N.A. Mohamed, J. Safaei,

A. Aadenan, S.N. Syed Nasir, A.F. Ismail, M.A. Mat Teridi, Ceram. Int. 45 (2019) 16797–16802.

[129] G. Rahman, O.S. Joo, Int. J. Hydrogen Energy 37 (2012) 13989–13997.

[130] S.N. Tijare, M. V. Joshi, P.S. Padole, P.A. Mangrulkar, S.S. Rayalu, N.K. Labhsetwar, Int. J. Hydrogen Energy 37 (2012) 10451–10456.

[131] K. Peng, L. Fu, H. Yang, J. Ouyang, Nat. Publ. Gr. (2016) 1–10.

[132] M. Humayun, Y. Qu, F. Raziq, R. Yan, Z. Li, X. Zhang, L. Jing, Environ. Sci. Technol. 50 (2016) 13600–13610.

[133] V.M. Gaikwad, J.R. Sheikh, S.A. Acharya, J. Sol-Gel Sci. Technol. 76 (2015) 27–35.

[134] V. Celorrio, K. Bradley, O.J. Weber, S.R. Hall, D.J. Fermín, ChemElectroChem 1 (2014) 1667–1671.

[135] V. Guigoz, L. Balan, A. Aboulaich, R. Schneider, T. Gries, Int. J. Hydrogen Energy 45 (2020) 17468–17479.

[136] Y. Gao, G. Yang, Y. Dai, X. Li, J. Gao, N. Li, P. Qiu, L. Ge, ACS Appl. Mater. Interfaces 12 (2020) 17364–17375.

[137] J. Pei, J. Meng, S. Wu, Q. Lin, J. Li, X. Wei, G. Han, Z. Zhang, J. Alloys Compd. 806 (2019) 889–896.

[138] J. Pan, Z. Jiang, S. Feng, C. Zhao, Z. Dong, B. Wang, J. Wang, C. Song, Y. Zheng, C. Li, Int. J. Hydrogen Energy 43 (2018) 19019–19028.

[139] X. Wang, Y. Liu, B. Ding, H. Li, X. Zhu, M. Xia, H. Fu, Sensors Actuators, B Chem. 276 (2018) 211–221.

[140] C. Liu, A. Piyadasa, M. Piech, S. Dardona, Z. Ren, P.X. Gao, J. Mater. Chem. C 4 (2016) 6176–6184.

[141] J. Ma, C. Lu, C. Liu, M. Qi, X. Xu, D. Yang, X. Xu, J. Alloys Compd. 810 (2019) 151845.

[142] C. Tuc Altaf, N.S. Sahsuvar, N. Abdullayeva, O. Coskun, A. Kumtepe, E. Karagoz, M. Sankir, N. Demirci Sankir, ACS Sustain. Chem. Eng. 8 (2020) 15209–15222.

[143] M. Zhang, G. Liu, D. Zhang, Y. Chen, S. Wen, S. Ruan, J. Alloys Compd. 602 (2014) 322–325.

[144] Y. Lee, T. Watanabe, T. Takata, M. Hara, M. Yoshimura, K. Domen, Bull. Chem. Soc. Jpn. 80 (2007) 423–428.

[145] C. Gómez-Solís, J.C. Ballesteros, L.M. Torres-Martínez, I. Juárez-Ramírez, Fuel 166 (2016) 36–41.

[146] J.M. Mora-Hernandez, A.M. Huerta-Flores, L.M. Torres-Martínez, J. Photochem. Photobiol. A

Chem. 391 (2020) 112363.

[147] L. Gao, Z. Li, J. Liu, RSC Adv. 7 (2017) 27515–27521.

[148] K. Wang, X. Wu, G. Zhang, J. Li, Y. Li, ACS Sustain. Chem. Eng. 6 (2018) 6682–6692.

[149] S. Bera, S. Ghosh, R.N. Basu, J. Alloys Compd. 830 (2020) 154527.

[150] L. Gao, X. Long, S. Wei, C. Wang, T. Wang, F. Li, Y. Hu, J. Ma, J. Jin, Chem. Eng. J. 378 (2019) 122193.

[151] G. Jia, L. Liu, L. Zhang, D. Zhang, Y. Wang, X. Cui, W. Zheng, Appl. Surf. Sci. 448 (2018) 254–260.

[152] H. Han, F. Karlicky, S. Pitchaimuthu, S.H.R. Shin, A. Chen, Small 15 (2019) 1902771.

[153] B. Zhang, G. Dong, L. Wang, Y. Zhang, Y. Ding, Y. Bi, Catal. Sci. Technol. 7 (2017) 4971–4976.

[154] G. Liu, Y. Li, Y. Xiao, D. Jia, C. Li, J. Zheng, X. Liu, Catal. Letters 149 (2019) 870–875.

[155] H. Wang, X. He, W. Li, H. Chen, W. Fang, P. Tian, F. Xiao, L. Zhao, Chem. Commun. 55 (2019) 11382–11385.

[156] H. Wang, X. He, L. Zhao, W. Li, H. Chen, W. Fang, P. Tian, Z. Huang, Z. Sun, J. Photochem. Photobiol. A Chem. 384 (2019) 111992.

[157] H. Song, Z. Sun, Y. Xu, Y. Han, J. Xu, J. Wu, T. Sun, H. Meng, X. Zhang, Sep. Purif. Technol. 228 (2019) 115764.

[158] J.W. Yoon, D.H. Kim, J.H. Kim, H.W. Jang, J.H. Lee, Appl. Catal. B Environ. 244 (2019) 511–518.

[159] M. Zargazi, M.H. Entezari, Electrochim. Acta 391 (2021) 138926.

[160] X. Peng, L. Ye, Y. Ding, L. Yi, C. Zhang, Z. Wen, Appl. Catal. B Environ. 260 (2020) 118152.

[161] G. Jia, L. Liu, L. Zhang, D. Zhang, Y. Wang, X. Cui, W. Zheng, Appl. Surf. Sci. 448 (2018) 254–260.

[162] J. Zhou, A. Zhou, L. Shu, M. Liu, Y. Dou, J. Li, Appl. Catal. B Environ. 226 (2018) 421–428.

[163] C. Mao, Y. Wang, W. Jiao, X. Chen, Q. Lin, M. Deng, Y. Ling, Y. Zhou, X. Bu, P. Feng, Langmuir 33 (2017) 13634–13639.

[164] N. Zhang, Y. Zhang, Y.J. Xu, Nanoscale 4 (2012) 5792–5813.

[165] M.H. Elbakkay, W.M.A. El Rouby, S.I. El-Dek, A.A. Farghali, Appl. Surf. Sci. 439 (2018) 1088–1102.

[166] S. Chandrasekaran, J.S. Chung, E.J. Kim, S.H. Hur, Chem. Eng. J. 290 (2016) 465–476.

[167] P. Subramanyam, T. Vinodkumar, D. Nepak, M. Deepa, C. Subrahmanyam, Catal. Today 325

(2019) 73–80.

[168] V. Thangaraj, J. Bussiere, J. Janot, M. Bechelany, M. Jaber, S. Subramanian, P. Miele, S. Balme, Eur. J. Inorg. Chem. 2016 (2016) 2125–2130.

[169] M. Öner, A.A. Çöl, C. Pochat-Bohatier, M. Bechelany, RSC Adv. 6 (2016) 90973–90981.

[170] S. Kawrani, A.A. Nada, M.F. Bekheet, M. Boulos, R. Viter, S. Roualdes, P. Miele, D. Cornu, M. Bechelany, Chem. Eng. J. 389 (2020) 124326.

[171] Y. Fang, I.S. Merenkov, X. Li, J. Xu, S. Lin, M.L. Kosinova, X. Wang, J. Mater. Chem. A 8 (2020) 13059–13064.

[172] S. Raheman A. R., R.S. Mane, H.M. Wilson, N. Jha, J. Mater. Chem. C 9 (2021) 8524–8536.

[173] J. Safaei, N.A. Mohamed, M.F. Mohamad Noh, M.F. Soh, N.A. Ludin, M.A. Ibrahim, W.N. Roslam Wan Isahak, M.A. Mat Teridi, J. Mater. Chem. A 6 (2018) 22346–22380.

[174] S. Kumar, S. Karthikeyan, A.F. Lee, Catalysts 8 (2018) 74.

[175] L. Wang, W. Si, Y. Tong, F. Hou, D. Pergolesi, J. Hou, T. Lippert, S.X. Dou, J. Liang, Carbon Energy 2 (2020) 223–250.

[176] N. Lei, J. Li, Q. Song, Z. Liang, Int. J. Hydrogen Energy 44 (2019) 10498–10507.

[177] N. Karjule, R. Phatake, M. Volokh, I. Hod, M. Shalom, Small Methods 3 (2019) 1900401.

[178] H. Yang, Q. Zhou, Z. Fang, W. Li, Y. Zheng, J. Ma, Z. Wang, L. Zhao, S. Liu, Y. Shen, Y. Zhang, Chem 7 (2021) 2708–2721.

[179] T. Zhao, Q. Zhou, Y. Lv, D. Han, K. Wu, L. Zhao, Y. Shen, S. Liu, Y. Zhang, Angew. Chemie - Int. Ed. 59 (2020) 1139–1143.

[180] Y. Zhang, M. Antonietti, Chem. - An Asian J. 5 (2010) 1307.

[181] A. Mohammad, M. Ehtisham, R. Karim, M. Hwan, Appl. Surf. Sci. 495 (2019) 143432.

[182] I.N. Reddy, L.V. Reddy, N. Jayashree, C.V. Reddy, M. Cho, D. Kim, J. Shim, Chemosphere 264 (2021) 128593.

[183] X. Huang, Z. Zeng, H. Zhang, Chem. Soc. Rev. 42 (2013) 1934–1946.

[184] C. Tan, H. Zhang, Chem. Soc. Rev. 44 (2015) 2713–2731.

[185] Z. Yin, H. Li, H. Li, L. Jiang, Y. Shi, Y. Sun, G. Lu, Q. Zhang, X. Chen, H. Zhang, ACS Nano 6 (2012) 74–80.

[186] T.H. Kim, Y.H. Kim, S.Y. Park, S.Y. Kim, H.W. Jang, Chemosensors 5 (2017) 15.

[187] K.C. Kwon, C. Kim, Q. Van Le, S. Gim, J.-M. Jeon, J.Y. Ham, J.-L. Lee, H.W. Jang, S.Y. Kim,

ACS Nano 9 (2015) 4146–4155.

[188] Z. Yin, B. Chen, M. Bosman, X. Cao, J. Chen, B. Zheng, Small 10 (2014) 3537-3543.

[189] Q. Pan, C. Zhang, Y. Xiong, Q. Mi, D. Li, L. Zou, Q. Huang, Z. Zou, H. Yang, ACS Sustainable Chem. Eng 6 (2018) 6378-6387.

[190] T.T. Nguyen, T.M. Cao, N.O. Balayeva, V. Van Pham, Catalysts 11 (2021) 857.

[191] W. Jian, X. Cheng, Y. Huang, Y. You, R. Zhou, T. Sun, J. Xu, Chem. Eng. J. 328 (2017) 474–483.

[192] D.D. Xia, F. Gong, X. Pei, W. Wang, H. Li, W. Zeng, M. Wu, D. V Papavassiliou, Chem. Eng. J. 348 (2018) 908-928.

[193] Y. Sang, Z. Zhao, M. Zhao, P. Hao, Y. Leng, H. Liu, Advanced Materials 27 (2014) 363-369.

[194] Y. Wen, Y. Xia, S. Zhang, J. Power Sources 307 (2016) 593–598.

[195] Z. Thiehmed, A. Shakoor, T. Altahtamouni, Catalysts 11 (2021) 1283.

[196] A. Ahmadi, M. Zargar Shoushtari, J. Electroanal. Chem. 849 (2019) 113361.

[197] M. Tayebi, Z. Masoumi, B. Lee, Ultrason. - Sonochemistry 70 (2021) 105339.

[198] D. Van Der Spoel, E. Lindahl, B. Hess, G. Groenhof, A.E. Mark, H.J.C. Berendsen, J. Comput. Chem. 26 (2005) 1701–1718.

[199] V. Stevanović, S. Lany, D.S. Ginley, W. Tumas, A. Zunger, Phys. Chem. Chem. Phys. 16 (2014) 3706–3714.

[200] J. Cheng, M. Sprik, Phys. Rev. B - Condens. Matter Mater. Phys. 82 (2010) 1–4.

[201] P. Zhou, H. Zhang, H. Ji, W. Ma, C. Chen, J. Zhao, Chem. Commun. 53 (2017) 787–790.

[202] M. Raju, S.Y. Kim, A.C.T. Van Duin, K.A. Fichthorn, J. Phys. Chem. C 117 (2013) 10558–10572.

[203] V. Viswanathan, H.A. Hansen, J. Rossmeisl, T.F. Jaramillo, H. Pitsch, J.K. Nørskov, J. Phys. Chem. C 116 (2012) 4698–4704.

[204] N.A.A. Rusman, M. Dahari, Int. J. Hydrogen Energy (2016) 1–19.

[205] P. Prachi R., W. Mahesh M., G. Aneesh C., Adv. Energy Power 4 (2016) 11–22.

[206] D.A.J. Rand, J. Solid state Electrochemistry 15 (2011) 1579–1622.

[207] U. Sahaym, E.M.G. Norton, J. Material Science 43 (2008) 5395–5429.

[208] S Atilhan, S Park, M M Halwagi, M Atilhan, M Moore, R B Nielsen, Current Opinion in Chemical Engineering 31 (2021) 100668

[209] S. Niaz, T. Manzoor, A.H. Pandith, Renew. Sustain. Energy Rev. 50 (2015) 457–469.

[210] H.T. Hwang, A. Varma, Curr. Opin. Chem. Eng. 5 (2014) 42–48.

[211] S.W. Jorgensen, Curr. Opin. Solid State Mater. Sci. 15 (2011) 39–43.

[212] R. Janot, M. Latroche, A. Percheron-Guégan, Mater. Sci. Eng. B Solid-State Mater. Adv. Technol. 123 (2005) 187–193.

[213] D. Schitea, M. Deveci, M. Iordache, Int. J. Hydrogen Energy 44 (2019) 8585-8600.

[214] K. Mazloomi, C. Gomes, Renew. Sustain. Energy Rev. 16 (2012) 3024–3033.

[215] C.J. Webb, J. Phys. Chem. Solids 118 (2014) 1240-1247.

[216] Q. Lai, M. Paskevicius, D.A. Sheppard, C.E. Buckley, A.W. Thornton, M.R. Hill, Q. Gu, J. Mao, Z. Huang, H.K. Liu, Z. Guo, A. Banerjee, S. Chakraborty, R. Ahuja, K.F. Aguey-Zinsou, ChemSusChem 8 (2015) 2789–2825.

[217] Y. Zhang, Z. Jia, Z. Yuan, T. Yang, Y. Qi, D. Zhao, J. Iron Steel Res. Int. 22 (2015) 757–770.

Figures

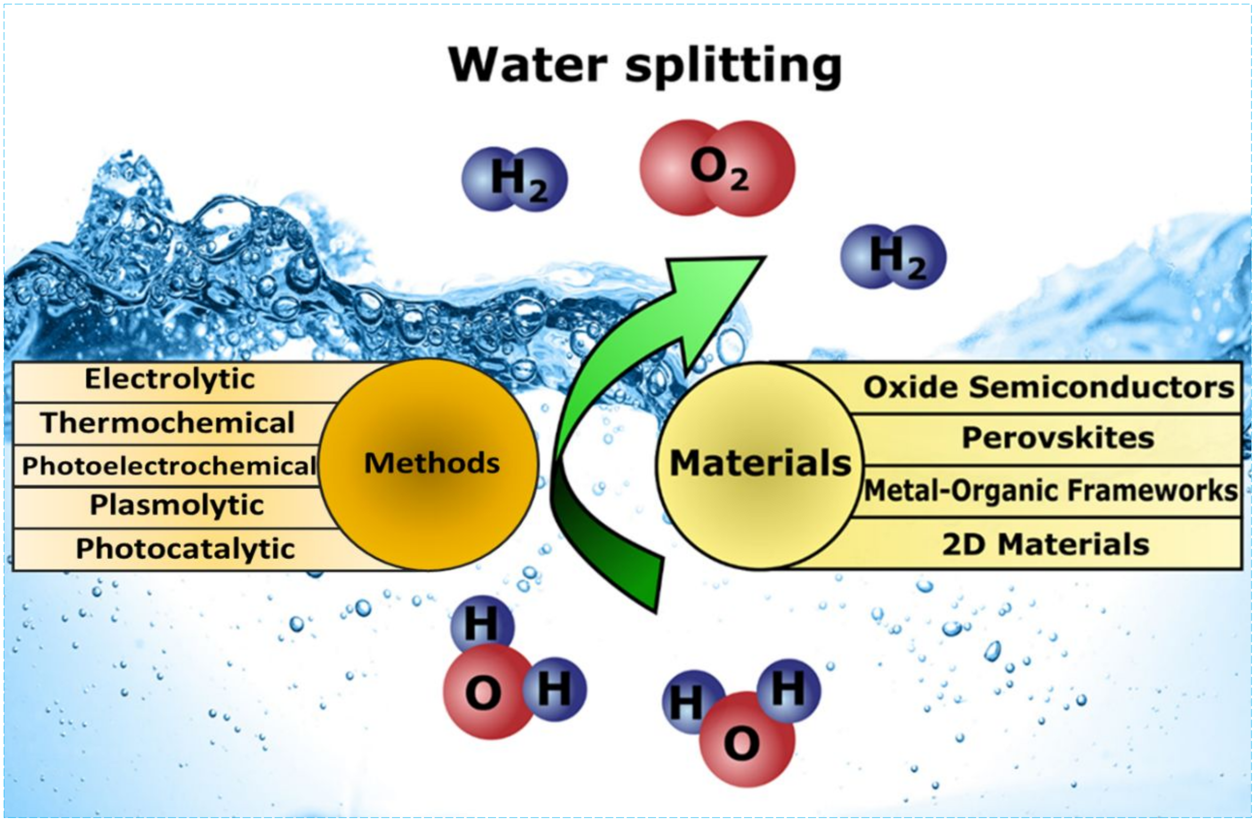

Figure 1. Overview of the multifunctional materials used for water splitting and types of water splitting

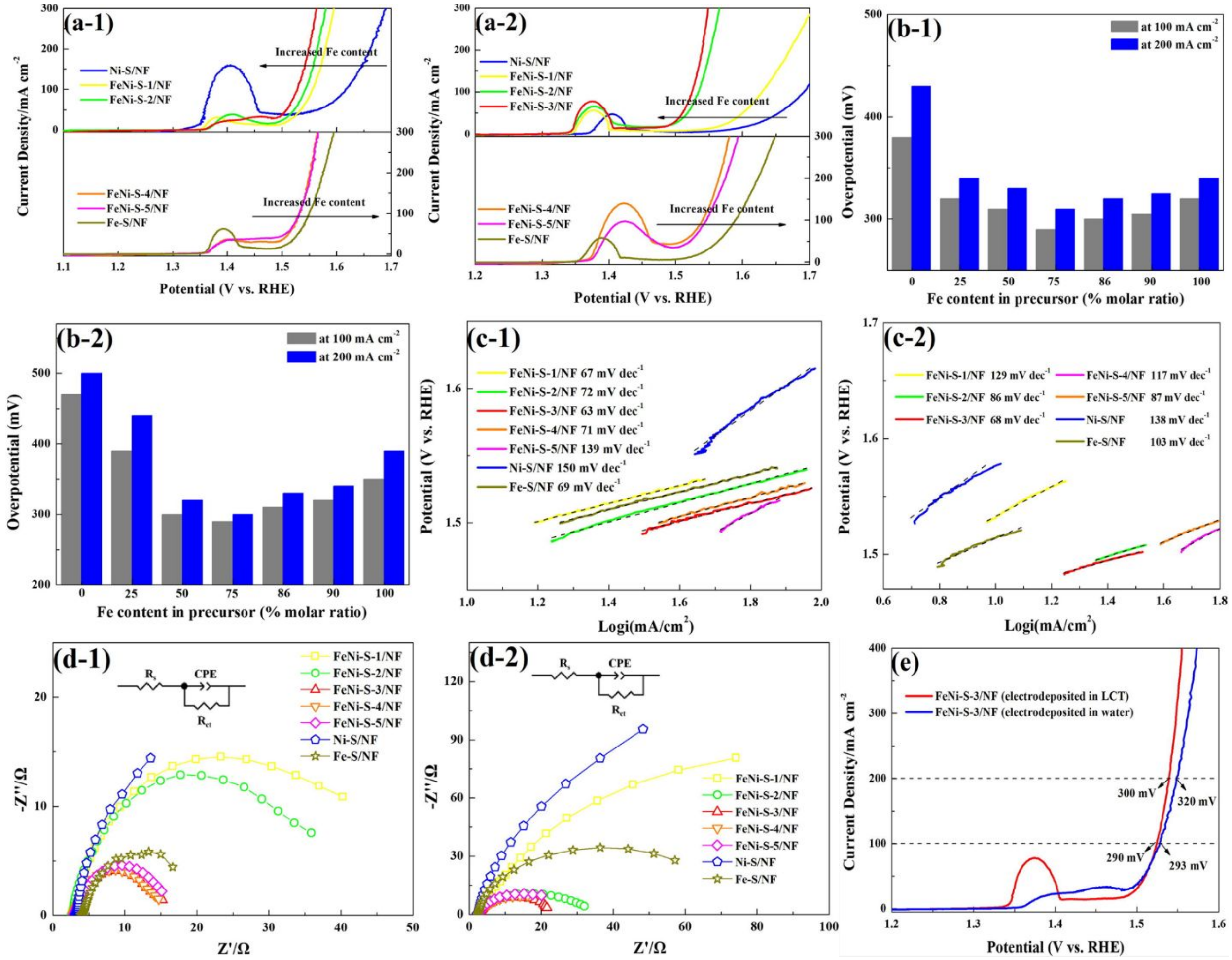

Figure 2. Electrochemical investigations of the binary Fe-Ni sulfides supported on nickel foam (FeNi-S/NF) with different composition ratios of Fe/Ni for HER in 1.0 M KOH. The labels FeNi-S-1/NF, FeNi-S-2/NF, FeNi-S-3/NF, FeNi-S-4/NF, and FeNi-S-5/NF refer to the Fe-Ni sulfides with the Fe/Ni molar ratios of 1/3, 1/1, 3/1, 6/1, 9/1, respectively. (a) Linear sweep voltammogram curves of the samples electrodeposited in (a-1) water solution and the LCT (a-2). (b) A comparison of overpotential at 10 and 100 mA cm^{-2}: electrodeposition in (b-1) water solution and (b-2) LCT; (c) Tafel plots of all samples electrodeposited in (c-1) water solution and LCT (c-2). (d) Electrochemical impedance spectroscopy of the samples electrodeposited in (d-1) water solution and (d-2) LCT. (e) Comparison of LSV of FeNi-S-3/NF deposited in water solution and LCT. Reprinted from [16] with permission from Elsevier. Copyright (2018) Elsevier.

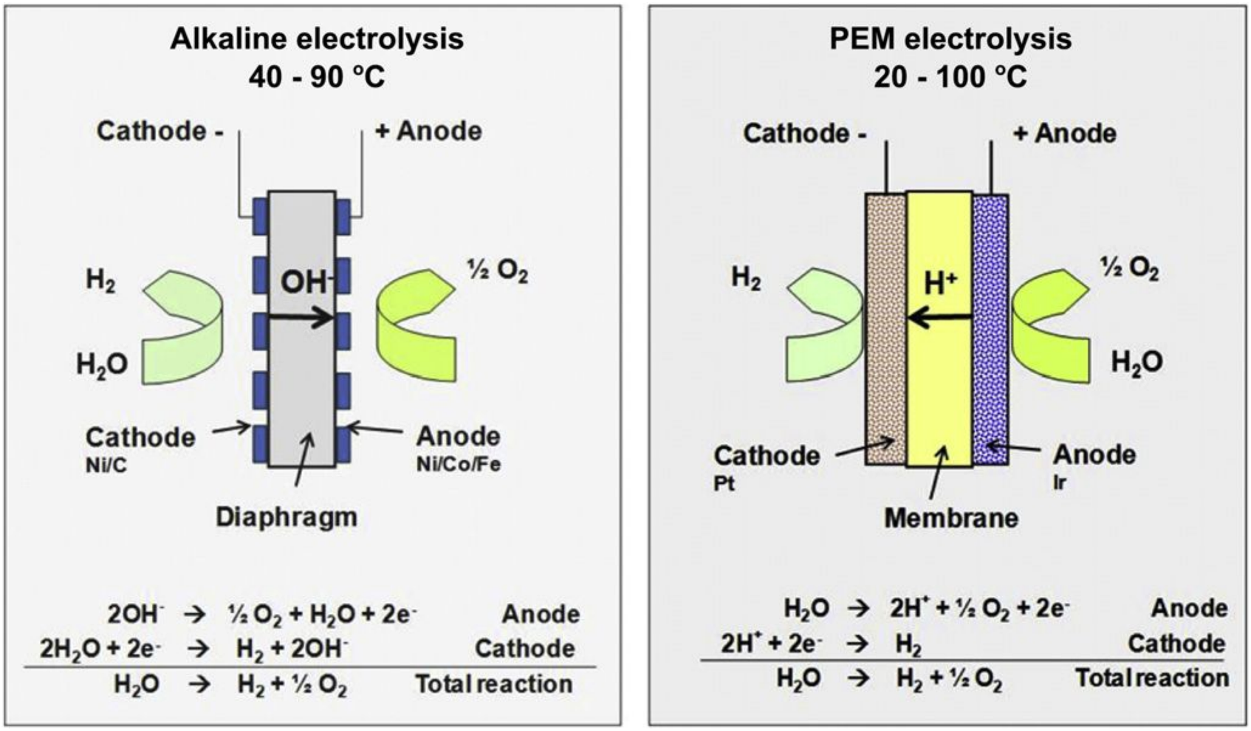

Figure 3. A comparison of the working principles of two different types of electrolyzers: alkaline (on the left) and PEM (on the right). A detailed description is provided in the text. Reprinted from [20] with permission from Elsevier. Copyright (2013) Elsevier.

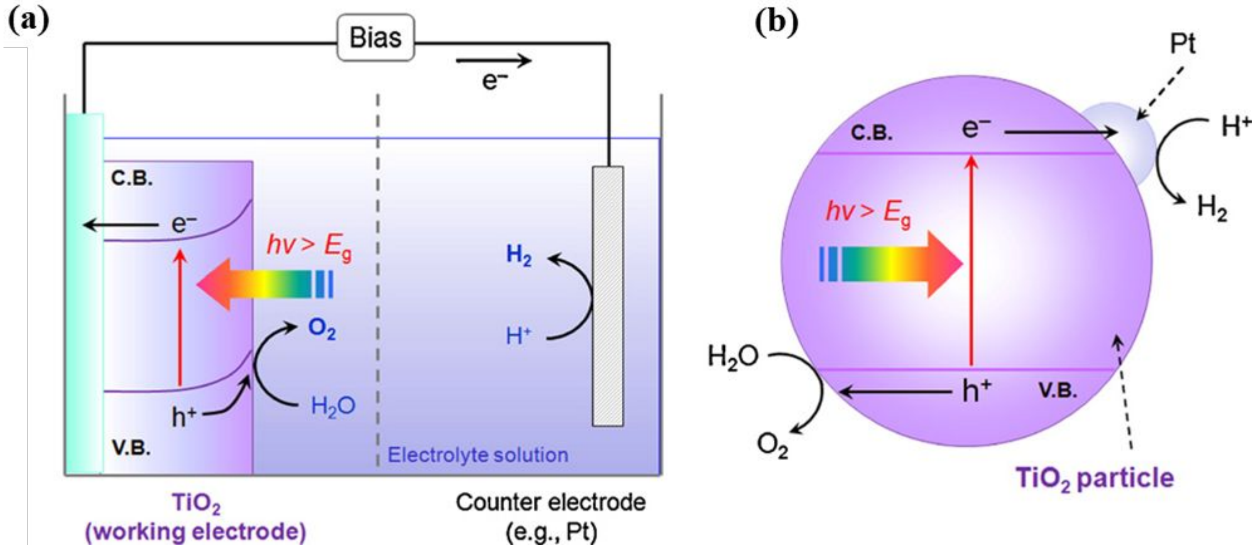

Figure 4. The schematic illustrations of (a) photo-electrochemical (PEC) cell and (b) PEC water splitting using the TiO_2 as a photoanode. A detailed description is provided in the text. Reprinted from [62] with permission from Elsevier. Copyright (2011) Elsevier.

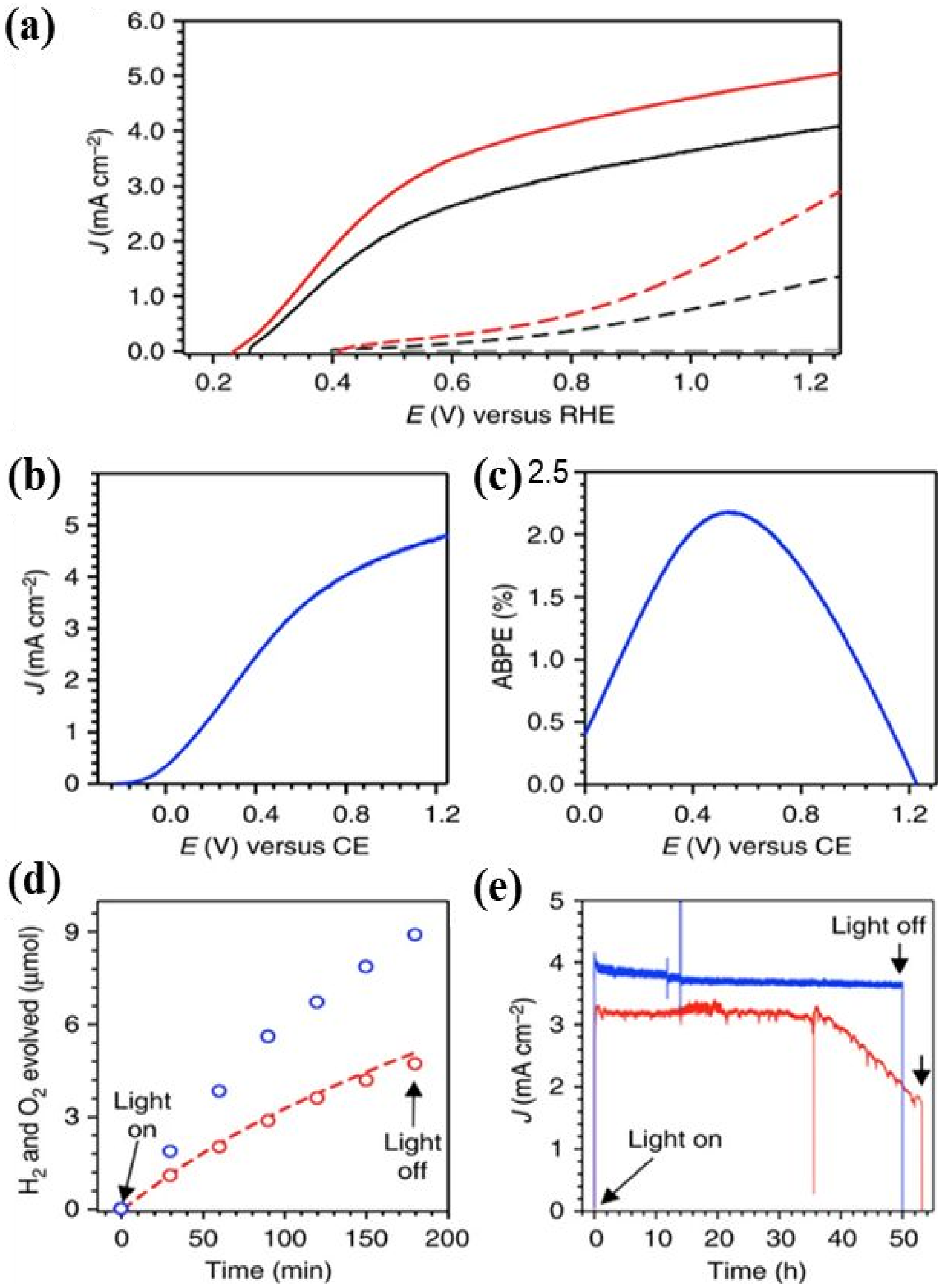

Figure 5. PEC water-splitting performance of pristine and nitrogen doped nanoporous bismuth vanadate electrodes. (a) J–V plots of $BiVO_4$/FeOOH/NiOOH (black solid curve), N_2-treated $BiVO_4$/FeOOH/NiOOH (red solid curve), $BiVO_4$ (black dashed line), and N_2-treated $BiVO_4$ (red dashed line) registered in a 0.5 M phosphate buffer under AM 1.5G illumination using a three-electrode cell. Grey dashed lines represent dark current of N_2-treated $BiVO_4$/FeOOH/NiOOH. (b) J–V plot and (c) applied bias photon-to-current efficiency (ABPE) of N_2-treated $BiVO_4$/FeOOH/NiOOH obtained using a two-electrode cell for solar water splitting (CE: counter

electrode). (d) Detection of hydrogen (blue points) and oxygen (red points) produced by N_2-treated $BiVO_4$/FeOOH/NiOOH at 0.6 V versus counter electrode. The red dashed line shows the amount of oxygen calculated assuming 100% Faradaic efficiency. (e) J–t plots of N_2-treated $BiVO_4$ for sulfite oxidation (blue curve) and N_2-treated $BiVO_4$/FeOOH/NiOOH for water oxidation (red curve) at 0.6 V versus RHE. Reprinted from [88] under a Creative Commons Attribution 4.0 International License (CC BY 4.0). Copyright (2015) Springer Nature.

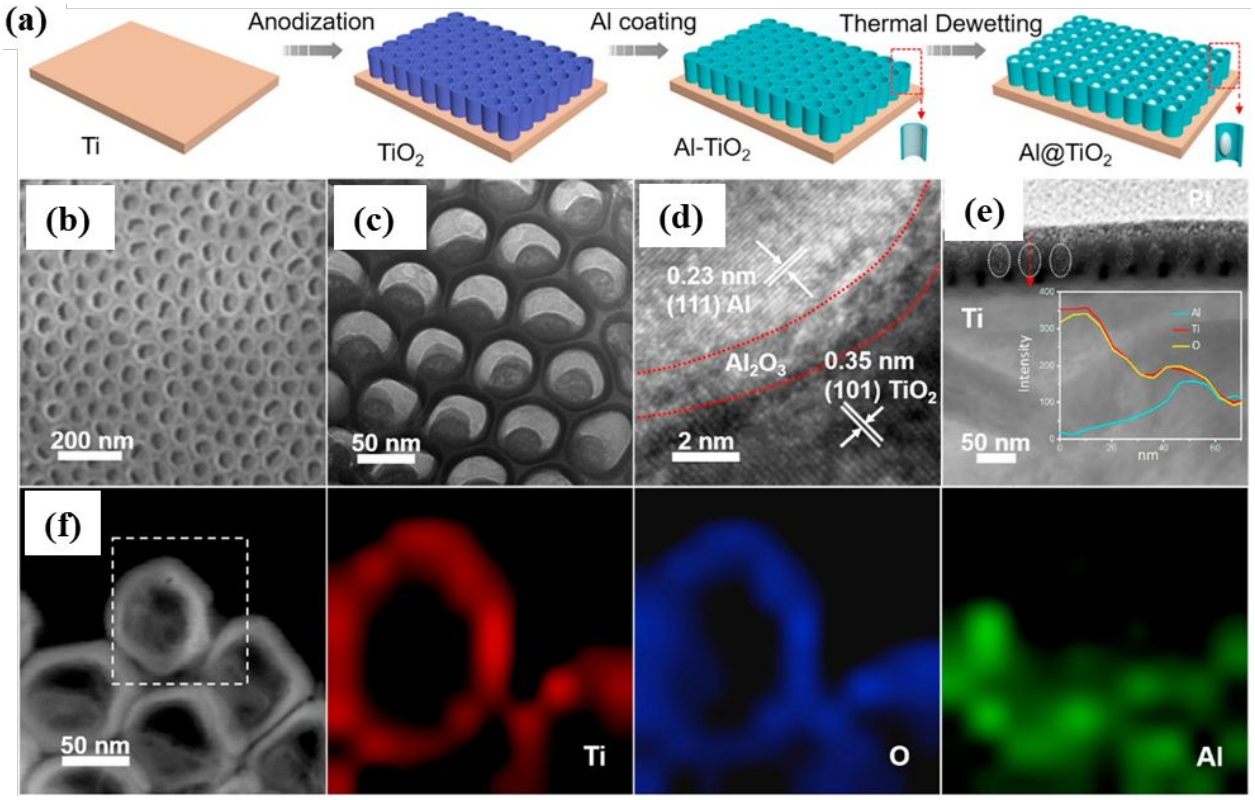

Figure 6. (a) A scheme presenting fabrication of plasmonic Al@TiO$_2$ heterostructures. (b) SEM, (c) TEM, (d) HRTEM, (e) cross-sectional STEM, (f) STEM and EDS mapping of Al@TiO$_2$. The inset in Fig. (e) presents the linear EDS profile captured from the red dashed line. Reprinted from [107] with permission from Elsevier. Copyright (2018) Elsevier.

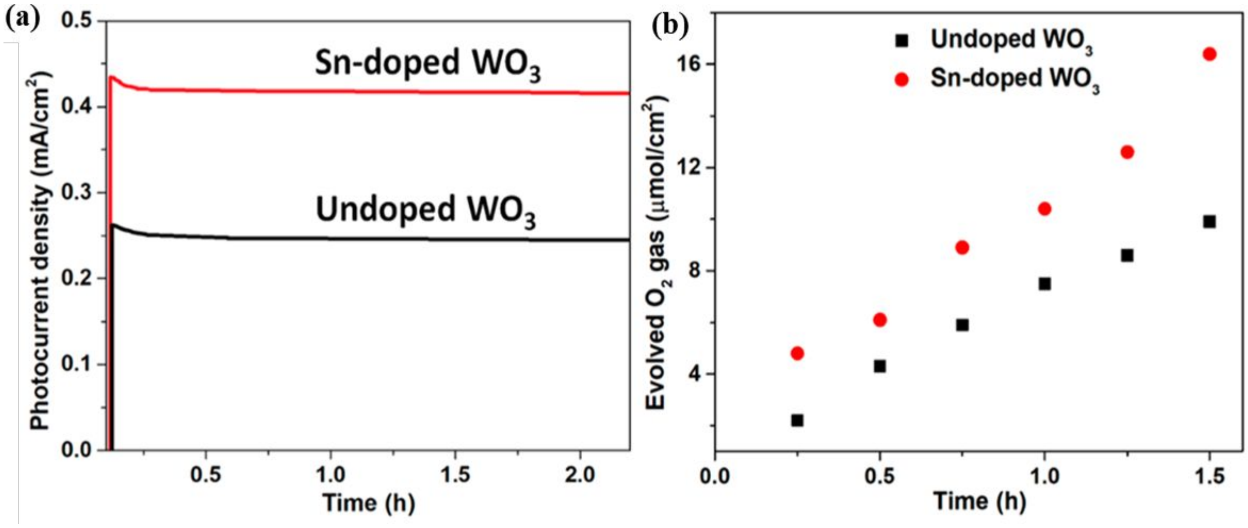

Figure 7. (a) The transient voltammograms of undoped and Sn-doped WO$_3$ thin films registered under AM 1.5 G illumination at a bias potential of 1.23 V RHE. (b) The evolution of oxygen gas at the photoanode for undoped and Sn-doped WO$_3$ under AM 1.5 G illumination measured at a bias potential of 1.23 V RHE. Reprinted from [110] under a Creative Commons Attribution 4.0 International License (CC BY 4.0). Copyright (2019) MDPI.

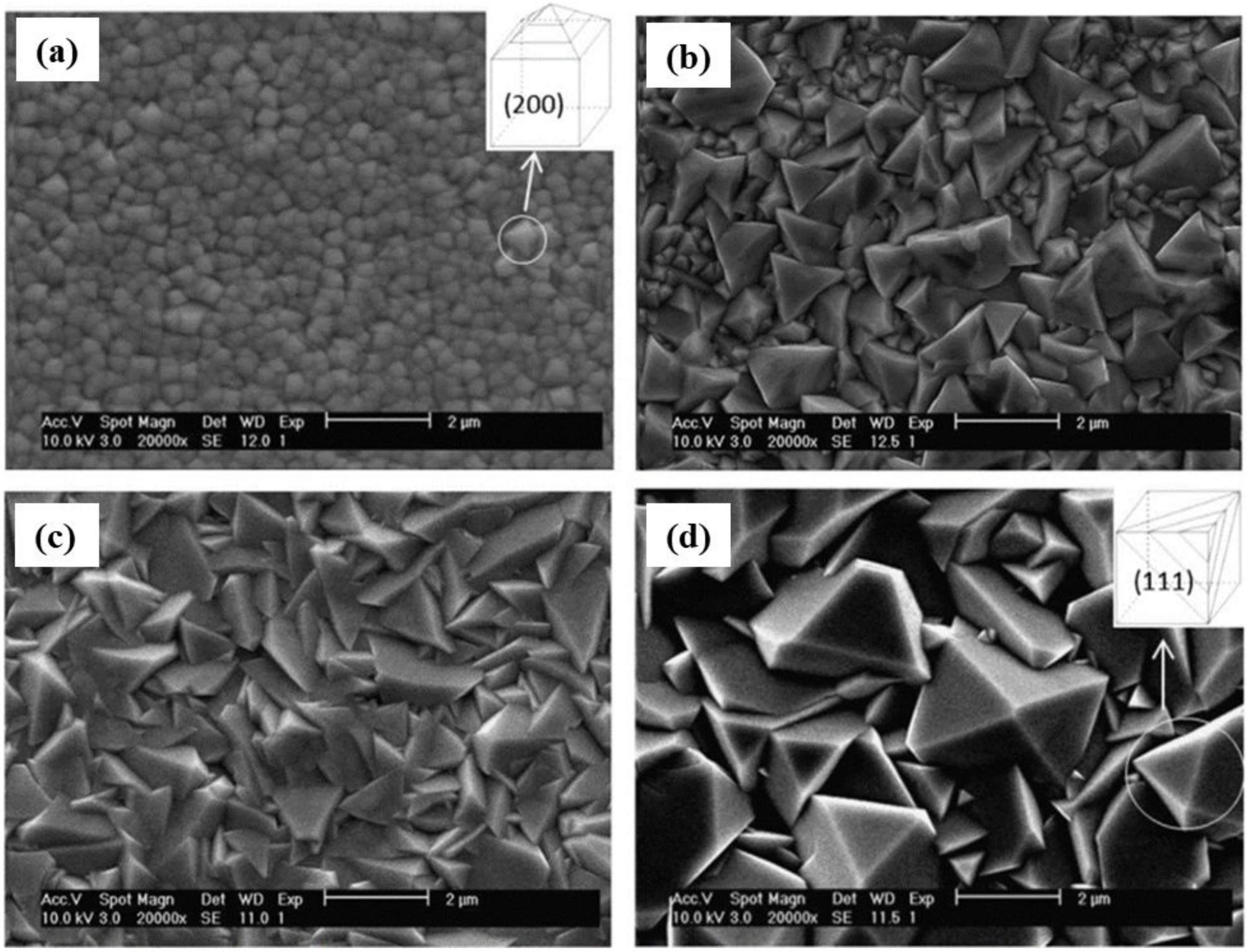

Figure 8. SEM micrographs of Cu_2O photoelectrodes prepared at various pH values: (a) pH=8; (b) pH=10; (c) pH=12; and (d) pH=14. Reprinted from [116] with permission from Elsevier. Copyright (2015) Elsevier.

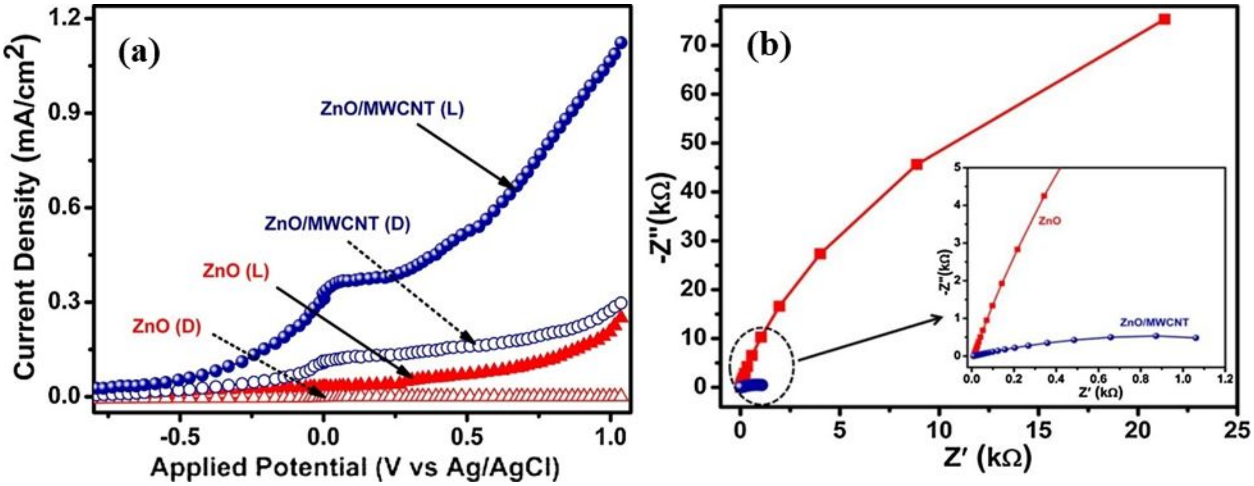

Figure 9. (a) The linear sweep voltammograms measure at applied potentials from −0.8 to +1 V (vs. Ag/AgCl) for pristine ZnO and ZnO/MWCNT in the dark (hollow spheres) and under the illumination of 100 mW/cm^2 (solid spheres). (b) EIS spectra of pristine ZnO and ZnO/MWCNT photoanodes. The inset in Figure (b) represents a zoom of the low impedance region. Reprinted from [120] with permission from Elsevier. Copyright (2018) Elsevier.

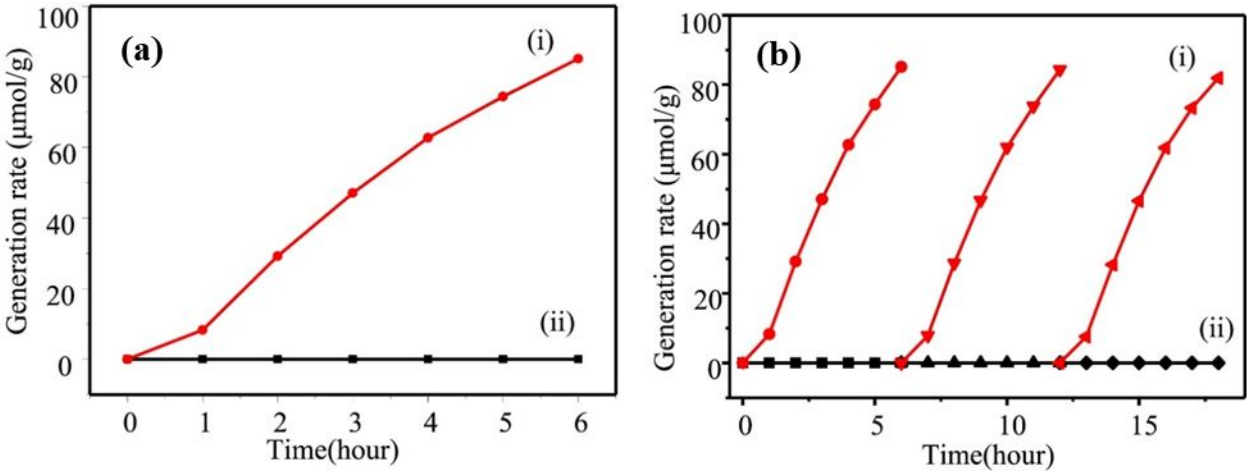

Figure 10. (a) Hydrogen generation rate and (b) cycling performance measured for $CaTiO_3$ nanoparticles synthesized with a polyvinyl alcohol concentration of (i) 8 g·L^{-1} and (ii) 0 g·L^{-1}. Reprinted from [137] with permission from Elsevier. Copyright (2019) Elsevier.

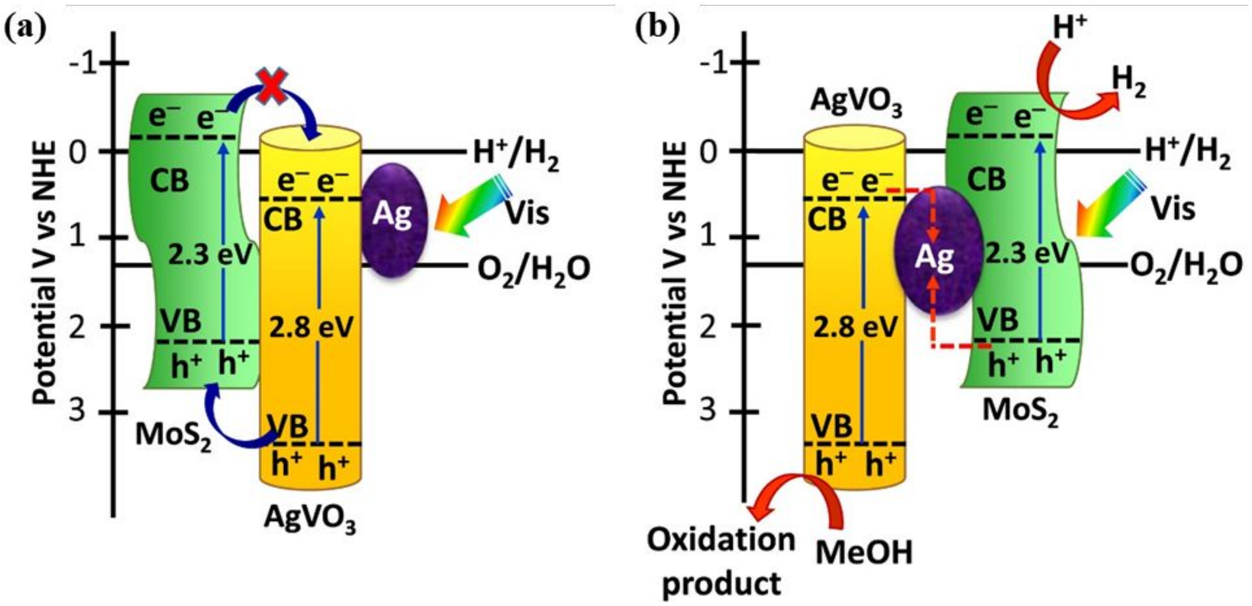

Figure 11. Possible interfacial charge-transfer mechanisms of (a) type II heterostructure and (b) Z-scheme heterostructure of MoS_2/Ag-$AgVO_3$ for photocatalytic H_2 generation under visible light irradiation. Detailed description is provided in the text. Reprinted from [149] with permission from Elsevier. Copyright (2020) Elsevier.

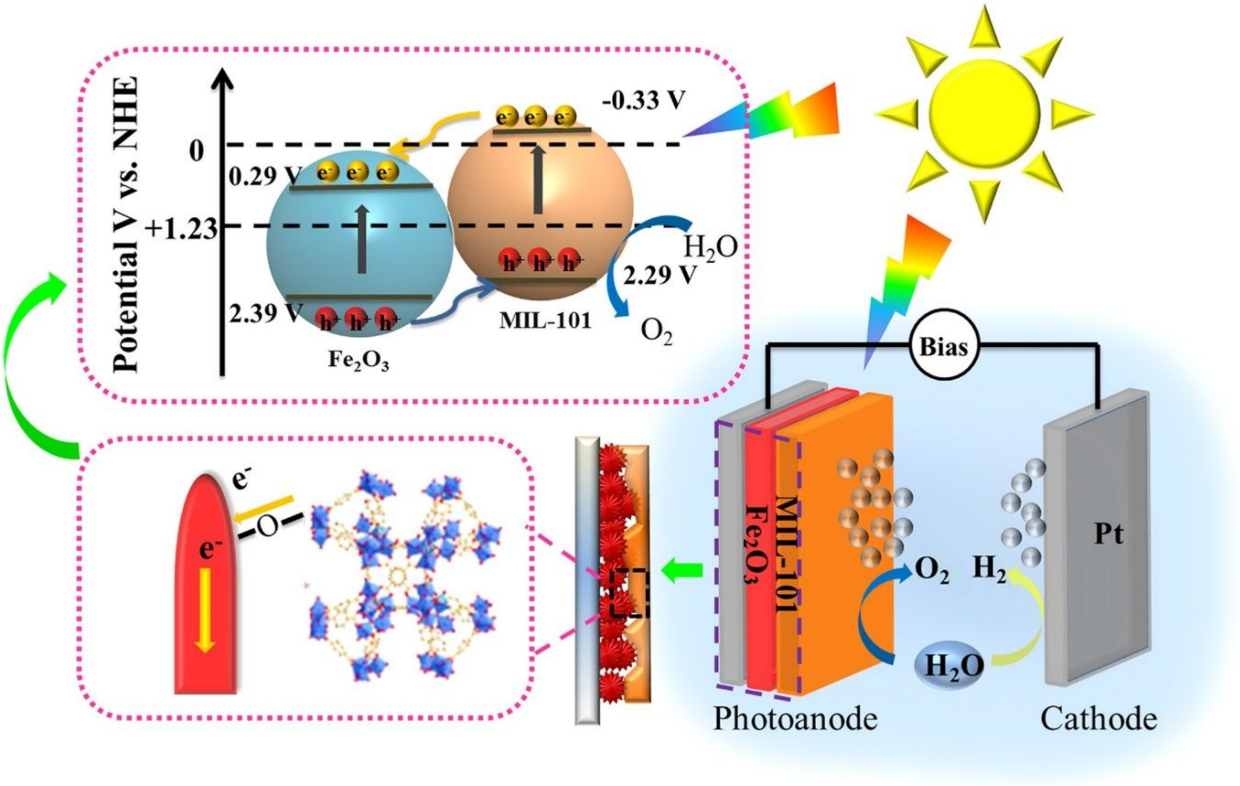

Figure 12. The schematic representations of energy band structure and electron transfer path of Fe_2O_3/MIL-101 heterojunction. Reprinted from [156] with permission from Elsevier. Copyright (2019) Elsevier.

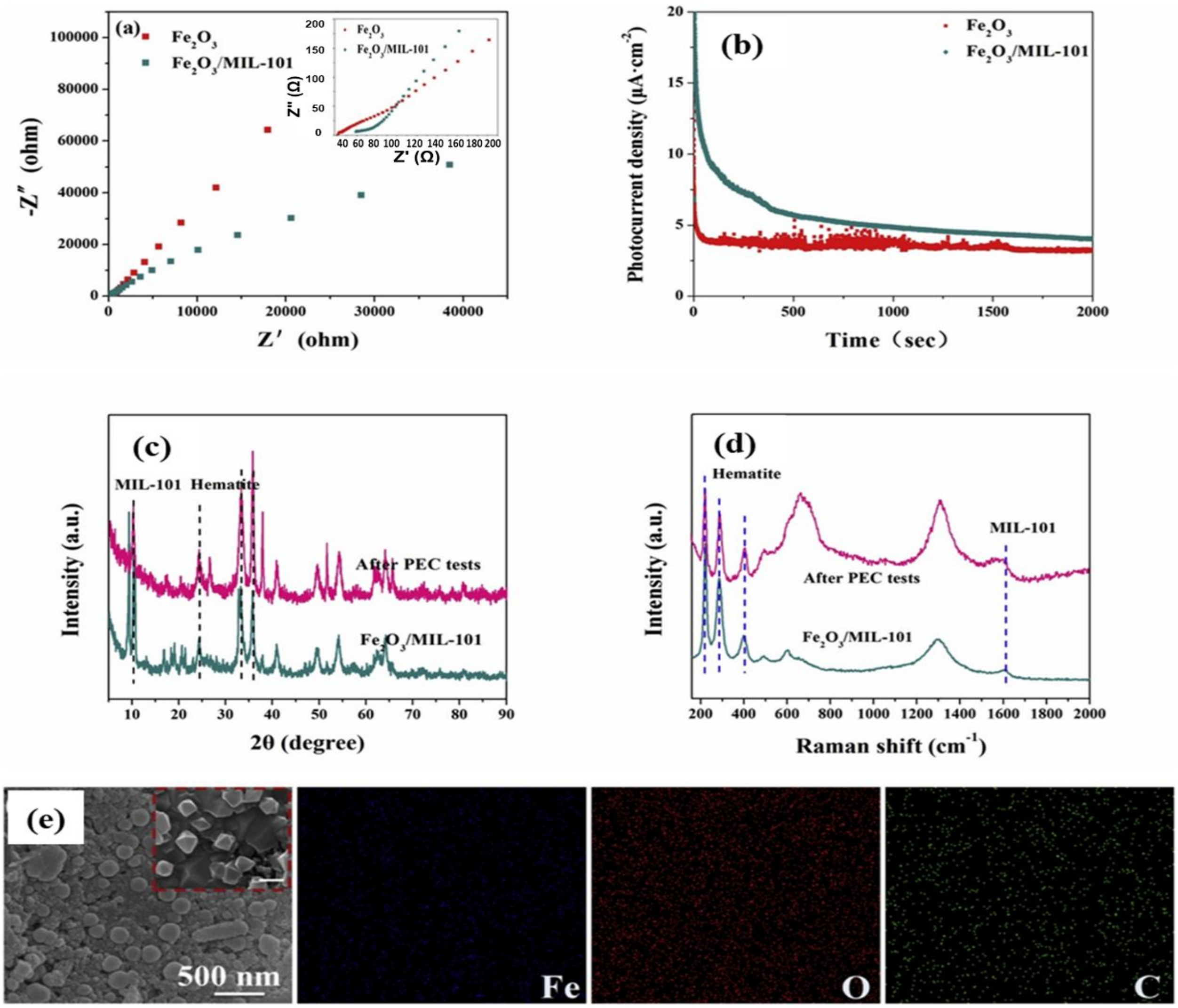

Figure 13. (a) EIS Nyquist plots, (b) Time dependence of photocurrent measured for Fe_2O_3 and Fe_2O_3/MIL-101 under continuous illumination at 0.6 V, (c) XRD patterns of Fe_2O_3/MIL-101 before and after PEC experiments, (d) Raman spectra of Fe_2O_3/MIL-101 before and after all PEC experiments, (e) SEM micrographs and EDX mapping images of Fe_2O_3/MIL-101 before (inset) and after PEC experiments. Reprinted from [156] with permission from Elsevier. Copyright (2019) Elsevier.

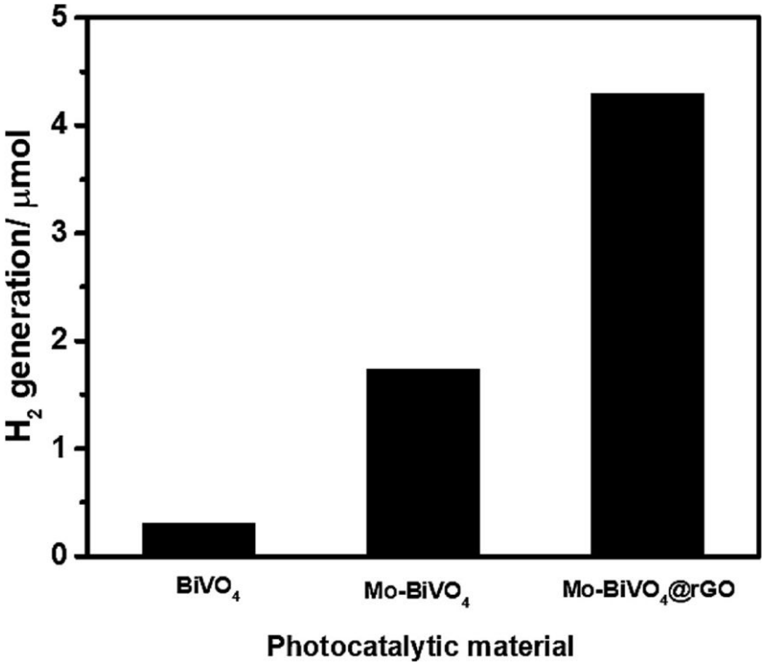

Figure 14. Hydrogen evolution was achieved for pure $BiVO_4$, molybdenum-doped $BiVO_4$ (Mo-$BiVO_4$), nanocomposite of molybdenum-doped $BiVO_4$, and reduced graphene oxide (Mo-$BiVO_4$@rGO) under solar light irradiation at zero potential after 3 hours of the experiment. Reprinted from [167] with permission from Elsevier. Copyright (2019) Elsevier.

Table 1: Comparison of various multifunctional materials, their light source, current density, and electrolyte for photoelectrochemical water splitting

Material	Synthesis method	Electrolyte	Light source	Current density	Reference
Ti–Ni–O nanotubes	Annealing	KOH	100 mW/cm^{-2}	0.93 mA/cm^2 vs. Ag/AgCl	[106]
Bi doped WO_3	Hydrothermal	0.1 M Na_2SO_4	AM 1.5 G	1.511 mA/cm^2 vs. RHE	[90]
Cu_2O/g-C_3N_4	Electrophoretic deposition	5.0 mol NaOH	100 mW/cm^{-2}	–1.38 mA/cm^2 vs. Ag/AgCl	[115]
ZnO/Au	Hydrothermal and photoreduction combined approach	0.1 M Na_2SO_4	100 mW/cm^{-2}	9.11 mA/cm^2 vs. Ag/AgCl	[121]
α-Fe_2O_3/ NiMn LDH	Solvent exfoliation	1 M NaOH	AM 1.5G	1.98 mA/cm^{-2} vs. RHE	[127]
$LaFeO_3$/g-C_3N_4	Magnetron sputtering	0.1 M Na_2SO_4	AM 1.5G	4 mA/cm^2 vs. Ag/AgCl	[135]
$ZnSnO_3$/MoS_2	Electrophoretic deposition method.	1 mol Na_2SO_4	xenon lamp	21.9 mA/cm^2 vs Hg/HgCl	[141]
RuO_2–$NaTaO_3$	Chronopotentiometry technique	0.5 M Na_2SO_4	AM1.5G	1.9 mA/cm^2 vs. RHE	[145]
MoS_2/Ag–$AgVO_3$	Co-precipitation method	0.5 M Na_2SO_4	100 mW/cm^{-2}	519 µA cm $^{-2}$ vs Ag/AgCl	[149]
ZnO@ZIF-8/67	Hydrothermal	0.5 M Na_2SO_4	AM 1.5 G	0.11 mA cm^{-2} vs. RHE	[151]
Mo:$BiVO_4$ - MIL-53(Fe)	Spin coating	0.2 M Na_2SO_4	AM 1.5G	1.67 mA cm^{-2} vs. RHE	[153]
Fe_2O_3/MIL-101	One-drop method under hydrothermal condition	0.01 M Na_2SO_4	AM 1.5 G	0.9 mA/cm^2 vs. Ag/AgCl	[156]
NH_2-MIL-125(Ti)/TiO_2	Hydrothermal	1 M NaOH	AM 1.5 G	1.63 mA/cm^2 vs. RHE	[158]
UiO-66/Pd/S,N GQDs	Hydrothermal	0.2 M Na_2SO_4	AM 1.5G	300 µA cm^{-2} vs. RHE	[159]
S-TiO_2/S-RGO	Solvothermal	1 M KOH	100 mW/cm^{-2}	3.36 mA/cm^2 vs. Ag/AgCl	[165]
2D Carbon Doped Boron Nitride	Plasma enhanced chemical vapor deposition	1.0 M NaOH	sunlight spectrum	120 µA/cm^2 vs REH	[155]
SnO_2-g-C_3N_4	Calcination	0.1 M KOH	100 mW/cm^{-2}	0.80 mA cm^{-2} vs RHE	[196]
MoS_2/$BiVO_4$	Electrochemical deposition and annealing	1 M Na_2SO_3	100 mW/cm^{-2}	2.72 mA cm^{-2} vs RHE	[196]
Ti and Mo doped WS_2	Chemical vapor deposition	0.05 M Na_2S	AM 1.5 G	10.44 mA/cm^2 vs RHE	[196]